

Geophysical constraints on the Luhoi (Tanzania) geothermal conceptual model



Egidio Armadillo^{a,*}, Daniele Rizzello^b, Claudio Pasqua^c, Paolo Pisani^c, Alessandro Ghirotto^a, Kato Kabaka^d, Taramaeli Mnjokava^d, Jonas Mwano^d, Makoye Didas^d, Lucas Tumbu^d

^a DISTAV, University of Genova, Italy

^b Tellus s.a.s., Italy

^c ELC-Electroconsult, Italy

^d Tanzania Geothermal Development Company Ltd (TGDC), Tanzania

ARTICLE INFO

Keywords:

Luhoi
Magnetotelluric survey
Gravimetric survey
Magnetic survey
Clay cation
exchange capacity
Geothermal conceptual model

ABSTRACT

We present the results of the gravimetric, magnetic and magnetotelluric geophysical campaign aimed to constrain the geothermal conceptual model of the Luhoi geothermal field, a poorly known system located in the Tanzanian southeastern coastal sedimentary basin. Regional assessment by existing potential field data reveals that Luhoi lies at the margin of a wide regional NE trending uplifted block that involves the Precambrian metamorphic basement complex. In the geothermal field area, 3D geophysical modelling has imaged a local asymmetric horst of Cretaceous age, 1 km wide and 5 km long, with the same regional NE trend. The horst is formed by the denser Kipatimu Lower Cretaceous sandstones surrounded by the Upper Cretaceous Ruaruke claystones that are down thrown up to 1 km by normal faulting. Far from the horst, lithology mainly controls the modelled electrical resistivity distribution: the Ruaruke claystones show low resistivity ($1\text{--}6 \Omega\text{m}$) primarily due to its clay content, while the Kipatimu sandstones have generally higher resistivity ($10\text{--}30 \Omega\text{m}$) because of their prevalent electrolytic conduction. However, anomalous low resistivity values ($1\text{--}5 \Omega\text{m}$) in the shallower portion of the Kipatimu sandstones forming the horst indicate enhanced electrical conduction due to the cation exchange capacity (CEC) of clay. The CEC estimated values from electrical resistivity are in the range $2\text{--}30 \text{ meq}/100 \text{ g}$, suggesting the presence of kaolinite and illite and excluding the occurrence of smectite, which is the typical clay mineral in the cap-rock of high-temperature geothermal systems. This shallow clay-rich layer together with the Ruaruke claystones act as a regionally continuous clay cap confining the reservoir formed by moderately hot water (close to 100°C from water geothermometers) in the permeable Kipatimu sandstones layer that reach a maximum depth of ca. 2 km, likely heated by a slightly enhanced geothermal flux attributable to crustal extension. At Luhoi, the local horst structure imaged by the geophysical models pushes up the sandstone reservoir at very shallow depth (about 500 m from the surface), strongly enhancing the local geothermal gradient and originating the surface thermal manifestations that are controlled by the system of normal faults.

1. Introduction

In the last decades, several reconnaissance surveys have provided basic information about the geothermal potential of Tanzania (Nzaro, 1970; SWECO, 1978; Hochstein et al., 2000; Mnjokava et al., 2015), while, in the recent years, different cooperative international projects have focused on detailed geoscientific surveys over the most promising prospect areas (Kabaka et al., 2016). Here we report about the high-resolution ground geophysical investigations of the Luhoi geothermal prospect carried out in 2017 together with new geological and geochemical surveys. The surface exploration studies discussed in this

paper were originally proposed to the Icelandic International Development Agency (ICEIDA) in the report by Hersir et al. (2015) as a result of an assessment of three areas in Tanzania.

The Luhoi geothermal prospect is located at the northern edge of the ESE trending Rufiji Trough, in the Tanzanian coastal basin, 60 km inland from the coast (Fig. 1b). The area is part of the proposed continuation (O'Donnell et al., 2013; Mulibo and Nyblade, 2016; Stamps et al., 2018) of the eastern branch of the East African Rift System that has been inferred to cross the Tanzanian coastal basin towards the ocean in front of southern Tanzania and Mozambique (Fig. 1a).

The Luhoi thermal manifestations comprise the hot springs of

* Corresponding author.

E-mail address: egidio@dipteris.unige.it (E. Armadillo).

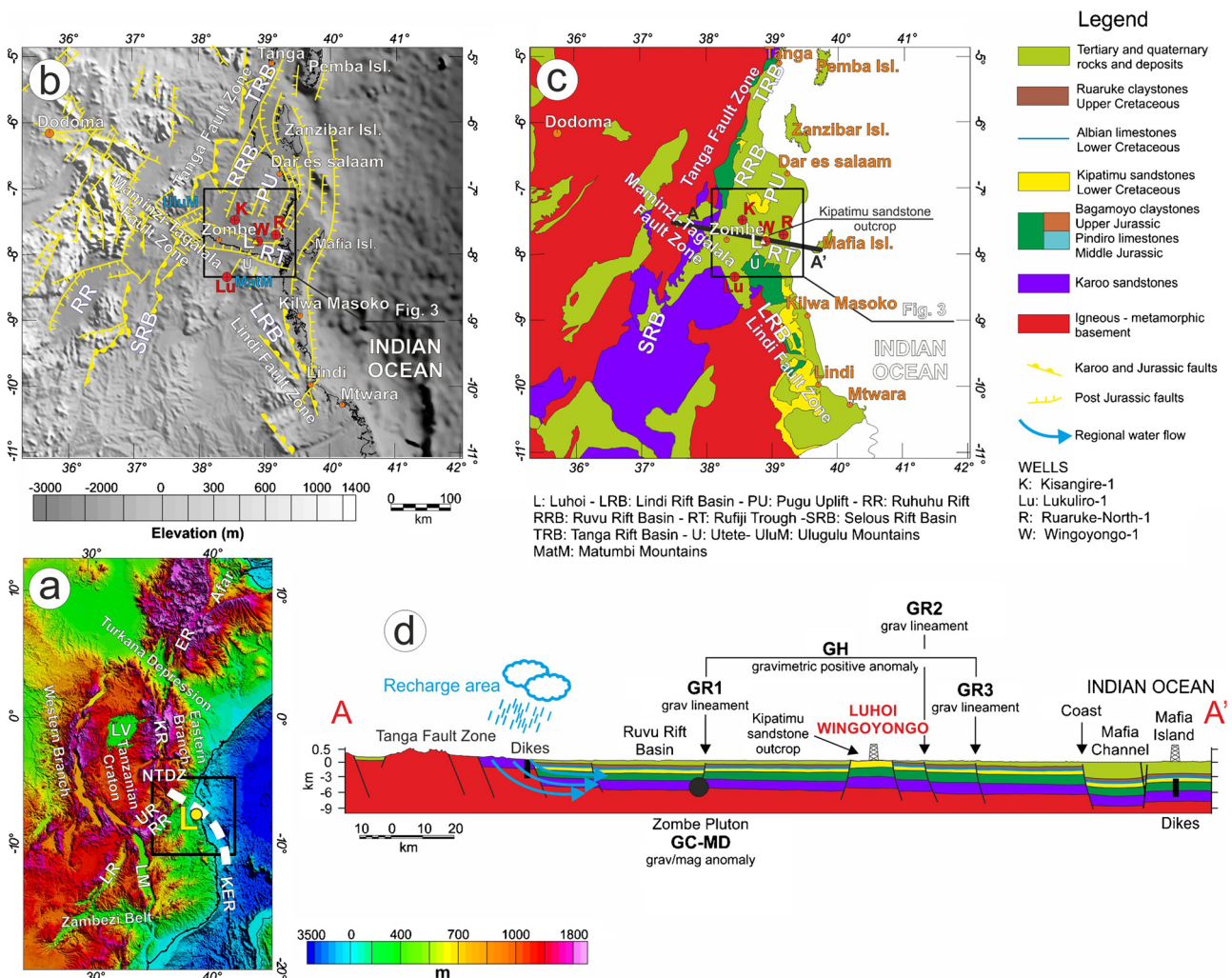


Fig. 1. Regional geological assessment. a) Topographic map of the East African Rift System (EARS). The heavy white dashed line represents the inferred prosecution of the eastern branch of the EARS (O'Donnell et al., 2013; Mulibio and Nyblade, 2016; Stamps et al., 2018). L: Luhoi; ER: Ethiopian Rift; KER: Kerimbas Rift; KR: Kenya Rift; LM: Lake Malawi; LV: Lake Victoria; LR: Luangwa Rift; NTDZ: Northern Tanzania Divergence Zone; UR: Usagaran Rift; RR: Ruhuhu Rift. b) Structural map from Kent et al. (1971) superimposed on theETOPO1 (Amante and Eakins, 2009) digital elevation model. c) Geological map modified from the Geological and Mineral Information System of the Geological Survey of Tanzania. Label explanations for panels b and c are reported in the figure below panel c. d) Geological section AA' (location in (b)); gravimetric lineaments and anomalies have been imported from Fig. 3; the vertical exaggeration factor in the elevation range -9 ± 0 km is 1.6 while in the range 0 ± 0.5 km is 9.6 to enhance the topographic features.

Nyongoni (with a conspicuous gas emission) and Mkolwa, both of Na-Cl composition and TDS of 6690 to 7250 mg/L, as well as the Wingoyongo gas vents (see Fig. 4 for a detailed location map). The Nyongoni and Mkolwa springs are located along the ESE flowing Ruhoi River, a tributary of the Rufiji River. At Nyongoni, the thermal water flows out from alluvial sediments depositing travertine and sulfur, whereas at Mkolwa the thermal water emerges from fractured quartzitic sandstones. These springs have a maximum temperature of 72 °C and an estimated total outflow of at least 25 L/s. As already suggested by Kraml et al. (2014), the chemical characteristics of these spring waters are derived by mixing between meteoric waters and seawater-like brines (either hosted in pores of sedimentary rocks or trapped in fluid inclusions), with estimated proportions of 98 to 83 % for meteoric waters and 2–17 % for seawater-like brines. To the Northeast, at about 5 km from the springs, the Wingoyongo (alternatively spelt Wingayongo) Hill forms a morphological high where emissions of H₂S-bearing gases and bituminous staining at the surface are observed. Here a bore hole (Wingoyongo-1) was drilled for petroleum exploration in 1954, revealing intense hydrothermal alteration in the shallower sandstone layers and rising of the drilling fluid temperature to 61 °C at 64 m depth (Kent et al., 1971).

The existing conceptual models of the Luhoi field are somehow contradictory and affected by large uncertainties. Some older investigations (Kent et al., 1971) suggested a probable volcanic heat source on the base of i) the igneous intrusion outcrops intruding the Karoo sediments in the middle Rufiji Trough (95 km to the West of Luhoi) and ii) the sills/dykes intruding the bottom of the Campanian mudstones in the Mafia Island deep borehole (95 km to the East). Preliminary resource evaluation carried out in 1998–2002 estimated a high reservoir temperature (over 200 °C) based on the Na-K-Ca geothermometer (Jica, 2014). On the base of new samples and analyses, Jica (2014) estimated a reservoir temperature of 183 °C (Na-K-Ca geothermometer) and hypothesized an intermediate depth reservoir presumably hosted in volcanic rocks but noted the lack of volcanic outcrops and features around Luhoi. On the contrary, a recent geochemical study by Kraml et al. (2014) modelled a low-temperature geothermal system (133 °C) with no geochemical indications in the water for a degassing magmatic heat source. The geochemical investigations in the frame of this project confirmed the expected low reservoir temperatures (close to 100 °C from water geothermometers) and the lack of any geochemical marker in the fluids indicating magmatic heat sources.

The geological structure and the distribution of faults in the

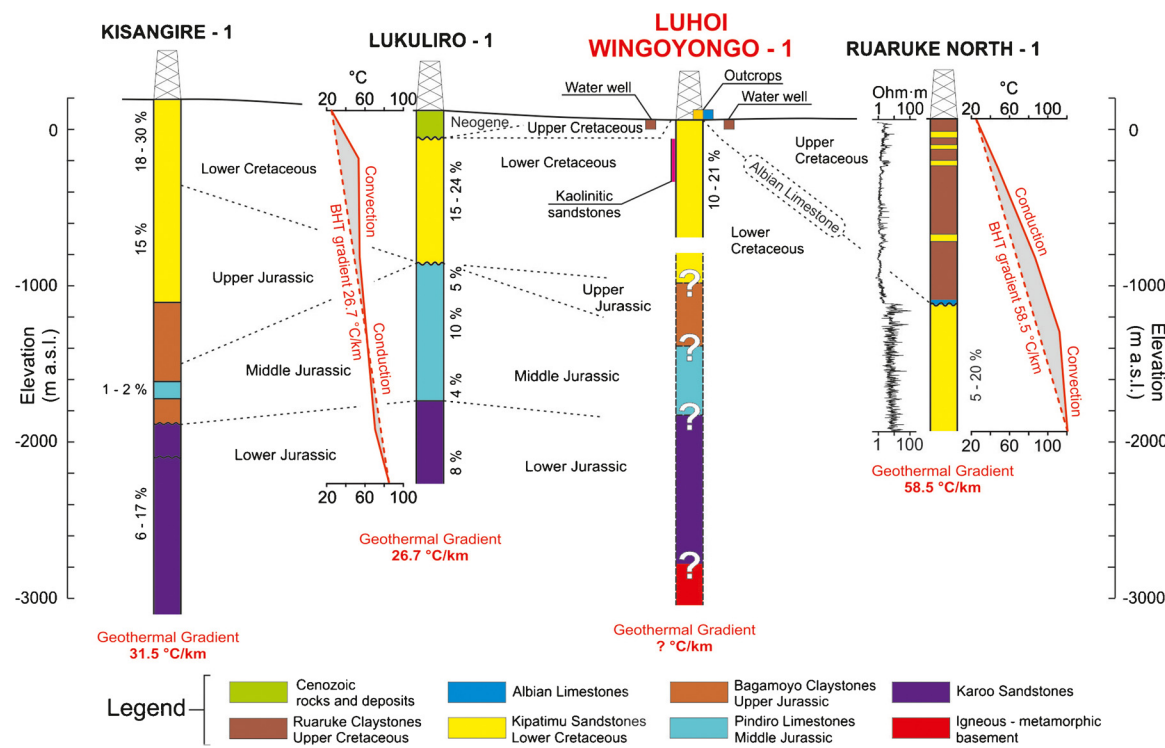


Fig. 2. Well stratigraphy and stratigraphic correlations at Kisangire-1, Lukuliro-1, Wingoyongo-1 and Ruaruke North 1 wells. Well locations are reported in Fig. 1. Measured porosities are labelled close to each well. The geothermal gradients computed from bottom hole corrected temperatures are reported when available as well as temperature-depth curves. Note the reduced geothermal gradient in the Kipatimu sandstones indicative of convection heat-flow. The resistivity log at Ruaruke North 1 well gives an estimation of the resistivity of the Ruaruke claystones ($2-6 \Omega\text{m}$) and of the Kipatimu sandstones ($8-16 \Omega\text{m}$). The unknown stratigraphy (dashed in the figure) below the Wingoyongo-1 hole bottom has been inferred from the other wells.

prospect area has remained largely unknown, due to the paucity of outcrops that prevents detailed structural and geological observations. Luhoi has been interpreted as a structural high by Kent et al. (1971) on the base of the surface and well evidence (outcropping Lower Cretaceous sandstones among post-cretaceous sediments, see the geological map in Fig. 1b and the sketch section in Fig. 2), but detailed structural information is not available. The Wingoyongo-1 well was stopped at a depth of 762 m, giving no information about the deeper stratigraphy below the outcropping sandstones (Fig. 2).

In order to improve our knowledge of the geothermal field, detailed magnetotelluric (MT), time-domain electromagnetic (TDEM), magnetic and gravimetric surveys have been carried out to obtain density and electrical resistivity models to be used as constraints for an improved geothermal conceptual model (Cumming, 2009).

2. Geological setting

The southeast coastal sedimentary basins of Tanzania (Fig. 1) is part of the hydrocarbon rich East African coastal basin, located in the western margin of the passive continental margin of the Indian Ocean. The basin is floored by the Neoproterozoic Pan-African metamorphic basement resulting from the East and West Gondwana amalgamation (e.g. Hanson, 2003). Given its petroleum potential (e.g. Zhou et al., 2013), the Tanzanian coastal basin has been studied from the 1950's mainly on the base of exploration wells, geological observations and seismic refraction and reflection surveys (Kent et al., 1971; Kajato, 1982; Mbede and Dualeh, 1997). In Fig. 1b we show a regional structural map superimposed on the digital elevation model of the area. The Tanzanian coastal basin is composed of two major Triassic-Lower Jurassic (Karoo time) rifts, the Selous-Ruvu-Tanga Rift (labelled SRB, RRB, TRB in the figure) and the Lindi Rift (LRB). The Rufiji Trough (RT), where Luhoi is located, is a more recent structure, likely of Neogene age according to Kent et al. (1971). These three sub-basins define the major

structural trends affecting the coastal region: i) the NE to NNE Tanga Trend; ii) the NNW Lindi Trend; iii) the ENE trend associated with the Rufiji Trough. Moreover, Le Gall et al. (2004) pointed out the importance of the WNW trending Maminzi–Tagalala fault zone as part of the suggested structural connection between the western and eastern branches of the East African Rift System throughout central Tanzania (via the Ruhuhu Rift, see Fig. 1a and b).

The geological map (Fig. 1c) shows the Precambrian gneissic basement underlying the syn-rift Mesozoic sediments associated to the East Africa passive margin onset and the Cenozoic sediments associated to the fluvio-deltaic system (Said et al., 2015). We have compiled a schematic stratigraphic section along the Rufiji Trough (Fig. 1d) on the base of the existing composed stratigraphic sections and columns of the Tanzanian coastal basin (Kent et al., 1971; Kajato, 1982; Mbede and Dualeh, 1997; Kapilima, 2002; Said et al., 2015), the evidence from the closest exploratory wells of Kisangire-1, Lukuliro-1, Wingoyongo-1 and Ruaruke-North-1 (see Fig. 2), the published seismic reflection sections crossing adjacent areas (Mpanda, 1997; Brownfield, 2016) and the lineaments inferred from our regional potential field data analysis (see Fig. 3 and paragraph 3). The section shows the regional uplift in the Luhoi area and confirms the structural interpretation of Kent et al. (1971).

The Permo-Triassic to Lower Jurassic fluvio-continental Karoo sandstones (interbedded with minor silts, claystones and evaporites) are the first onset of sedimentary rocks that unconformably overlie the Precambrian gneissic basement (Fig. 1c). At Lukuliro-1 the Karoo sandstones have been intersected at 1800 m depth (Fig. 2), showing a porosity of 8%; at Kisangire-1 they have been found at 2070 m depth with porosity in the range 6–17%. In the Middle Jurassic a first marine transgression overlapped the continental Karoo sediments, with deposition of shallow water limestones (Pindiro limestones in the Lukuliro-1 well) and, in the Late Jurassic, marine shales, clay and marls (Bagamoyo claystones in the Kisangire-1 well) were deposited. Log

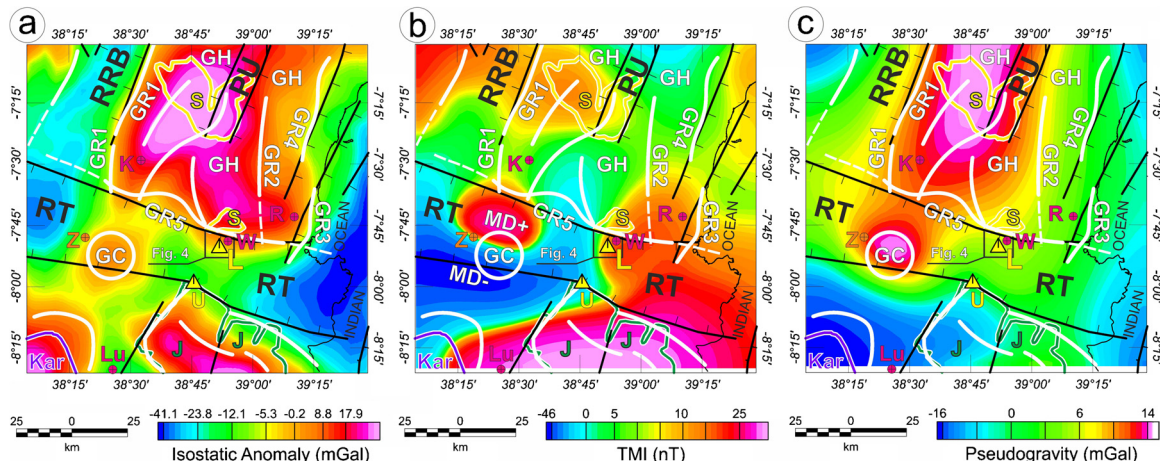


Fig. 3. Regional geophysical assessment. a) Isostatic anomaly computed from the free air anomaly of the World Gravity Map compilation (Bonvalot et al., 2012); gravimetric lineaments (white lines GR1–GR5) have been traced over the local maxima of the horizontal gradient; GH is a wide gravimetric high that we interpret as the signature of the regional basement uplift; GC is a circular anomaly interpreted as due to a cold pluton at 4–8 km depth. The surface geothermal manifestations at Luhoi (L) and Utete (U) are marked by triangles. b) Total magnetic intensity (TMI) anomaly from the EMAG2 data (Meyer et al., 2017); note the dipolar anomaly MD. c) Pseudogravity transform (e.g. Blakely, 1995) of the TMI that removes the dipolar magnetic effect of sources; the gravimetric lineaments of (a) have been superimposed on pseudogravity and show a good correlation in the area of the Rufiji Trough and to the North of it, suggesting the same sources for gravimetric and magnetic anomalies in these areas. S, J and Kar indicate the outcrops of Kipatimu sandstones, Jurassic claystones / limestones and Karoo sediments respectively. Z indicates Zombe town. Other labels are defined in the legend of Fig. 1.

porosities of the Pindiro limestones are in the range 4–10 %. In the Lower Cretaceous, regressive sands (Kipatimu sandstones) were deposited in an area comprising Wingoyongo-1 (porosity 12–15 %), Lukuliro-1 (15–24 %) and Ruaruke-North-1 (5–20 %). They outcrop at Luhoi and extensively to the North (see Figs. 1b and 2). At the end of the Lower Cretaceous, in the Aptian-Albian, a new transgressional cycle originated a thin limestone layer visible in a small outcrop at Luhoi and drilled at the Ruaruke-North-1 well (Fig. 2). Superimposed on the thin limestone layer, Albian and Upper Cretaceous deep marine sediments were deposited, consisting mainly of claystones (Ruaruke claystones) with lenses of fine sandstones as visible at Ruaruke-North-1 (Fig. 2). At Luhoi the Upper Cretaceous Ruaruke claystones have been found in some shallow water wells (Kent et al., 1971). From the Eocene a new regressive phase occurred giving shales and sandstones, while in the Rufiji area a deltaic continental sedimentation prevailed (Said et al., 2015).

At Luhoi, we found two small outcrops of the thin Albian limestones (Fig. 2). Petrographic analysis shows a fine to very fine sandy texture with a modal estimated volume close to 80 % of micritic and sparry calcite and about 20 % of accessory minerals (quartz and opaques). Outcrops of the Kipatimu sandstone unit occur in the form of scattered and small exposures located mostly along the Ruhoi River. The outcrops show jointing characterized by centimetric spacing (5–10 cm) with main orientation WNW (Tagalala trend) and sub-vertical dip angles. Petrographic analysis indicates that the rock is a fine to medium grained quartz arenite, consisting mostly of quartz grains with presence of clay (10 %), opaques (5%) voids (10 %) and traces of alkali feldspar, amphibole and mica. The stratigraphic column of the Wingoyongo-1 well (Fig. 2) shows that the Kipatimu sandstones reach the hole bottom at 762 m. Faultlets dipping at 70° with 5 cm throw are frequent in the hole, and most joints dip at vertical to 70° often with 0.5 cm open fissures (Kent et al., 1971). In Fig. 2 we have drawn the expected stratigraphic column below the well bottom from the data acquired in the Lukuliro-1 and Kisangire-1 wells drilled in the neighbours. Thicknesses reported in the expected stratigraphic column are the mean values between Lukuliro-1 and Kisangire-1 wells. Note that the Pindiro limestones or the Bagamoyo claystones might be eroded, similarly to the stratigraphy of Lukuliro-1 and Kisangire-1 wells.

3. Regional geophysical data

To infer the geological regional structure around Luhoi, we have interpreted the World Gravity Map (WGM) compilation (Bonvalot et al., 2012) and the Total Magnetic Intensity (TMI) magnetic EMAG2 data (Meyer et al., 2017). Possible source of the long wavelength gravimetric signal may be faulting that causes horizontal density contrast between the denser gneiss basement (expected density of 3000 kg/m³ from direct measurements in the Southwest of Tanzania by Rizzello et al., 2018) and the post Permian to Quaternary sediments (expected density range 2200–2600 kg/m³ from Daly et al., 1966) or between claystones (2200–2400 kg/m³) and sandstones (2400–2600 kg/m³). Other plausible anomaly sources may be dykes that have been found close to Luhoi in some outcrops (see Fig. 1c) intruding Karoo sediments 95 km to the West or in the Mafia Island well below the Campanian mudstones (Kent et al., 1971). Density of intrusions (sills, dykes or batholiths) is expected to be higher than the Permian to Quaternary sediments but not higher than the basement density and therefore they may be detected only in the case they intrude the sediment column. Also, for the magnetic signal possible anomalies sources may be the horizontal magnetization contrast due to faulting between the metamorphic basement against the post Permian to Quaternary sediments presumably with very low susceptibility. The Karoo sediments derive from the dismantling of the basement rocks and therefore their magnetization contrast with the basement is expected to be low. Intrusions with prevalent induced or normal polarity residual magnetization are expected to give a magnetic dipolar anomaly with the positive lobe to the North, since the mean inclination of the external magnetic field at Luhoi is -38.3°. Both magnetic and gravimetric anomalies may also be generated by shallow mineral alterations, but the detectability of these signals in this long wave-length regional data set is unlikely.

For the gravity data, we first applied the terrain correction to the WGM free air data with standard reference density of 2670 kg/m³ and then the isostatic Airy correction (i.e. with zero elastic thickness) assuming a compensation depth of 35 km, standard crustal density of 2670 kg/m³ and mantle density of 3300 kg/m³. The resulting isostatic anomaly map is shown in Fig. 3a. We interpret the positive gravimetric regional anomaly trending NE labelled GH in the map as the signature of the regional horst-like structure outlined in the sketch section of Fig. 1c. The horst master faults (labelled GR1, GR2, GR3 and GR4) have

been traced by picking the horizontal derivative maxima of the isostatic anomaly. These faults appear to be the continuation of some mapped Tanga Trend faults (see also Fig. 1) and a structural connection with the mapped Pugu Uplift (PU) is plausible.

Close to the Luhoi manifestations, at the intersection with the Rufiji Trough, the quick drop of the positive isostatic anomaly towards SW suggests that the regional horst structure is strongly down-thrown by a WNW trending fault system (GR5) that marks the northern flank of the Rufiji Trough. In the Rufiji Trough, close to Zombe (labelled Z), a circular gravimetric anomaly GC indicates the presence of an isolated source. South of the Rufiji Trough other WNW trending anomalies are visible. They may be linked to the neogenic Rufiji trend or, as suggested by Kent et al. (1971), may represent the local geophysical signature of the WNW trending Utete lineament interpreted as a first order older discontinuity in the basement. However, these anomalies are difficult to be interpreted without other constraints.

The total magnetic anomaly (TMI) shown in Fig. 3b is downward continued at the sea level (Meyer et al., 2017). Note that the circular isostatic anomaly GC is centred in the middle of a corresponding dipolar magnetic anomaly MD with positive lobe to the North, indicating induced and/or normal polarity remnant magnetization. In Fig. 3c we show the pseudogravity transform of the TMI (Blakely, 1995) that removes the dipolar effects and enlightens the horizontal location of the magnetic sources. In this map the regional horst-like structure mapped by gravity (GH in Fig. 3a) has a correspondent pseudogravity positive signature, indicating that the uplift movement likely reaches the Precambrian gneissic basement giving a magnetization contrast with the post Permian sediments. The horizontal location of the magnetic dipole MD is well focused over the gravity GC anomaly, indicating a unique source. The same magnetic anomaly MD has been interpreted as the signature of a possible intrusion by Kent et al. (1971) on the base of old aeromagnetic data. The match between the gravimetric and magnetic anomalies shown here strongly supports this interpretation. We have estimated the source depth by Spector and Grant (1970) and Euler deconvolution (Reid et al., 1990) methods obtaining a range of 4–8 km. The magnetic signature implies that the intrusion temperature is below the Curie temperature (approximative mean value 550 °C, e.g. Li et al., 2017). Moreover, no thermal manifestations are known close to Zombe. Since some volcanic intrusions and carbonatite outcropping in the region have been attributed to Cretaceous or Karoo age (Kent et al., 1971), we conclude that the Zombe pluton body is cold and cannot represent the heat source of the Luhoi system. The crustal isotopic signature of the noble gases dissolved in the Nyongoni hot spring waters (Kraml et al., 2014) confirms this interpretation, excluding contributions from the mantle or from actively degassing magmatic heat sources.

In conclusion, regional potential field analysis combined with the geological and structural evidence (Fig. 1a and b) suggests that the Luhoi field is located at the margin of a wide regional NE trending uplifted block (marked by the gravimetric high GH in Fig. 3a) that involves the basement metamorphic complex (Fig. 1c). This block is downthrown by the ESE trending Rufiji Trough.

4. Geophysical methods and models

4.1. The gravimetric survey

A gravimetric survey was performed consisting of 124 gravity stations collecting data on a dense grid with 800 m of nominal spacing and 16 sparse stations located within 20 km from Luhoi to sample the regional field for residual anomalies computations (locations of these 16 stations are not shown in Fig. 4). We used a G927 LaCoste & Romberg gravity meter with nominal sensitivity of 10 µGal, equipped with electronic levels and nulling system. Daily measurements were referred to a base station for instrument drift correction. The measures error was estimated by repeated measurements at some survey stations giving a

mean error of 31 µGal. The gravity survey was associated with a differential Global Navigation Satellite System (GNSS) topographic survey with an average vertical component error of 3.2 cm.

After the standard drift, tide, normal gravity, free-air and topographic corrections, we computed the Bouguer anomaly with a reference density of 2400 kg/m³ that is the estimated density of the Kipatimu sandstone outcropping at Wingoyongo. As digital elevation model, we used the ASTER (NASA/METI/AIST/Japan Spaceystems and U.S./Japan ASTER Science Team, 2009) data, with 30 m resolution, integrated with our GNSS measurements, extending 10 km away from the survey area. At larger distance we used theETOPO1 (Amante and Eakins, 2009) data with 1 arc minute resolution, extending 300 km beyond the survey area. The final estimated mean error of the Bouguer anomaly is 44 µGal. We have estimated the regional gravity field including the 16 stations located within 20 km from the survey area. The final residual Bouguer map obtained removing the regional field from the computed Bouguer anomaly is shown in Fig. 5a. The map shows an elongated positive anomaly trending NE with maxima values over 3 mGal that lowers towards NW and SE to values below -2 mGal. We traced the gravimetric lineaments shown in Fig. 5 (G1-G6, continuous white lines) by picking the Bouguer anomaly horizontal gradient maxima. The gravimetric trends are associated with several lineaments detected by remote sensing analysis (black lines in the figure).

The residual Bouguer anomaly map can be interpreted considering that the Lower Cretaceous Kipatimu sandstones (estimated density 2400 kg/m³) outcrop at Wingoyongo (Figs. 1b and 2) and that the Upper Cretaceous Ruaruke claystones (2250 kg/m³) were found in some shallow water wells (maximum depth 30 m, Fig. 2) at a few kilometres to the East and West of Wingoyongo (Kent et al., 1971). On the base of this stratigraphic information, Kent et al. (1971) suggested the presence of some unknown faults down-throwing the claystones with respect of the uplifted sandstones. We therefore interpret the detected gravimetric lineaments trending NE and marking the edge of the NE trending positive anomaly as the signature of this inferred fault system.

Three-dimensional inverse modelling of the residual Bouguer anomaly data was carried out by means of a software package that implements the algorithm of Parker (1972) operating in the wave-number domain. According to our gravimetric interpretation, we set a simplified two-layers initial model assuming fixed 2400 kg/m³ (Kipatimu sandstones) and 2250 kg/m³ (Ruaruke claystones) densities for the lower and upper layer respectively. We assigned a starting uniform depth of 0.5 km to the sandstone-claystone interface on the base of Spector and Grant (1970) and 3D Euler Deconvolution (Reid et al., 1990) depth estimations applied to the residual Bouguer anomaly map. These depth estimations also indicate that other possible deeper density contrasts have a negligible effect on the measured gravimetric anomaly. During inversion, changes to the layer interfaces occur iteratively to minimise the data misfit while the density contrast is maintained fixed.

We show the claystone layer thickness derived from the final 3D model in Fig. 5b. The map images an asymmetric horst-like structure trending NE affecting the Kipatimu sandstones that outcrop in the region of the Wingoyongo hill (dark blue area). The Ruaruke claystones are downthrown by the horst master faults with a maximum slip of the order of 1 km. The orientation of the imaged local horst structure resembles the orientation of the regional trends and uplifted blocks shown in Fig. 1c. Therefore, it can be interpreted as a local feature of a wider regional fault system (Fig. 3) generating the regional uplift.

Immediately at NE and SW of the Nyongoni/Mkolwa springs (white circles in Fig. 5) the horst is strongly downthrown by two inferred WNW trending faults marked by dashed white lines (labelled S1 and S2). These faults have a good correlation with some lineaments imaged by remote sensing (black lines). This WNW structural trend is also visible in the NW sector of the survey area, where a gravimetric lineament (G6) shows a similar trend to the WNW remote sensing lineaments.

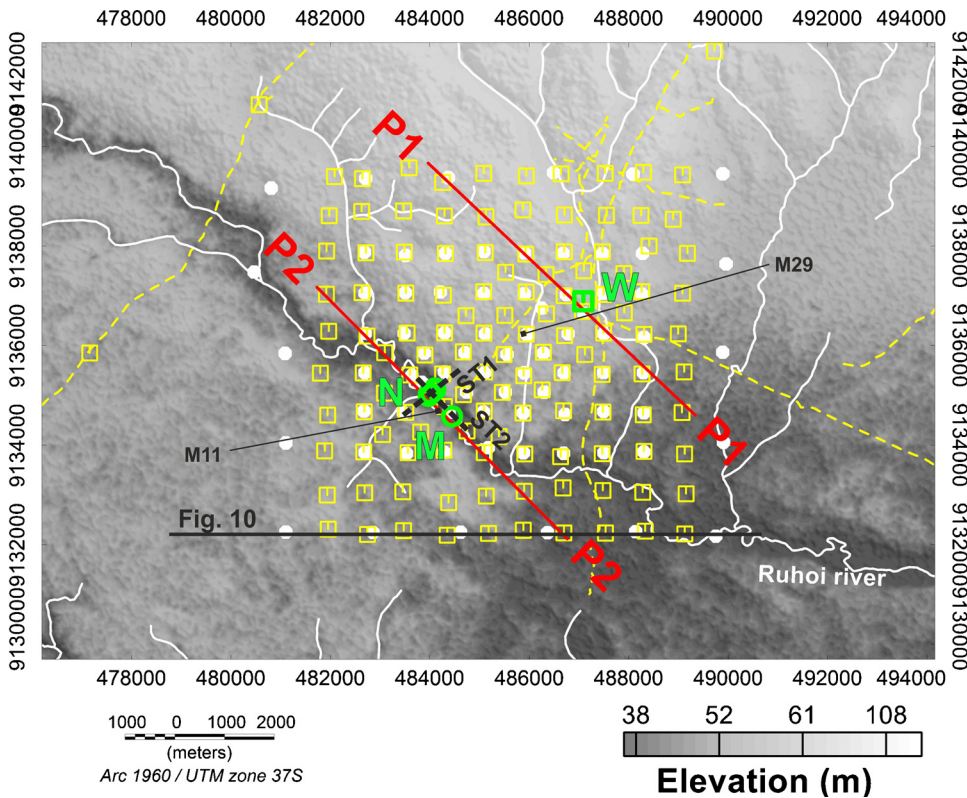


Fig. 4. Location of the 124 gravimetric stations (yellow squares) and 76 MT/TDEM stations (white circles) superimposed on the ASTER digital elevation model of the area (NASA/METI/AIST/Japan Spacesystems and U.S./Japan ASTER Science Team, 2009). White lines: rivers. Labels N, M and W indicate the Nyongoni, Mkolwa and Wingoyongo manifestations respectively. P1 and P2 are the traces of the profiles shown in Fig. 11. Dashed black line ST1 indicates the NE alignment of the thermal manifestations at Nyongoni; ST2 indicates the W-NW alignment between the Nyongoni and Mkolwa manifestations. Magnetotelluric data at stations M11 and M29 are shown in Fig. 7. The EW black line indicates the location of the resistivity pseudo-2D profile shown in Fig. 10. (For interpretation of the references to colour in this figure legend, the reader is referred to the web version of this article).

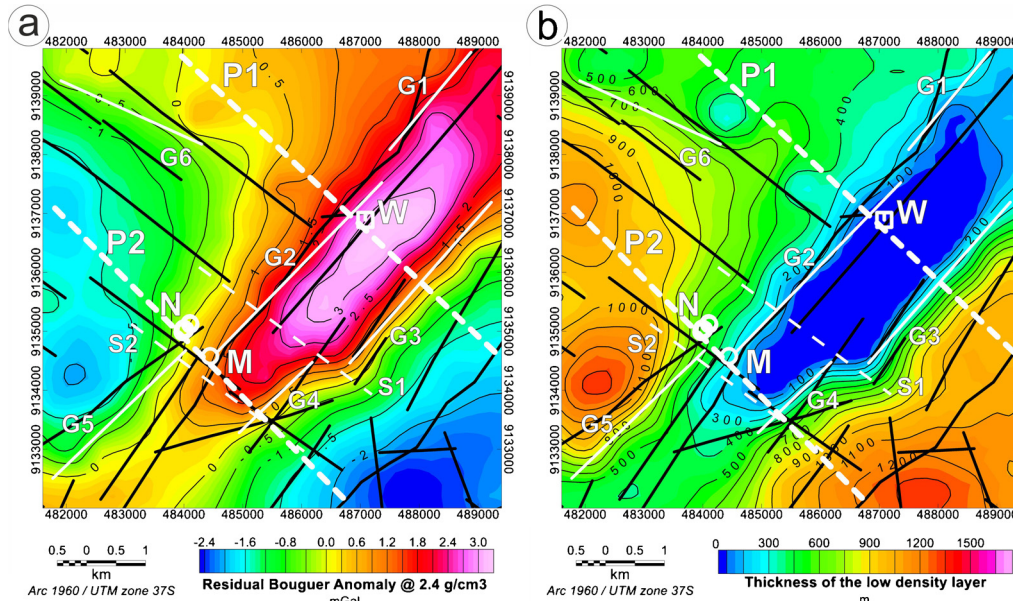


Fig. 5. Gravimetric survey results. a) Residual Bouguer anomaly; gravimetric lineaments G1-G6 have been traced following the local maxima of the horizontal gradient. b) Thickness of the shallow low density layer derived from the 3D gravimetric inversion, interpreted as the Ruaruke claystones (2250 kg/m^3) superimposed on the Kipatimu sandstones (2400 kg/m^3); the pattern depicts a horst structure trending NE. Dashed light lines S1 and S2 are inferred faults that down-throw the horst to the SW. Black lines are the major lineaments derived by remote sensing analysis. Labels N, M and W indicate the Nyongoni, Mkolwa and Wingoyongo manifestations, respectively. Dashed heavy white lines labelled P1 and P2 indicate the traces of the profiles shown in Fig. 11.

4.2. Magnetotelluric and time domain electromagnetic survey

The magnetotelluric (MT) dataset comprised 76 five-components stations (white circles in Fig. 4) distributed over an area of approximately 75 km^2 . Electric and magnetic field time series at each site were acquired in the $1000 - 0.0001 \text{ Hz}$ range by means of two broadband systems with an average record length of 21 h at each station. A third MT reference station was located about 20 km to the North of the survey area. Impedances and vertical magnetic transfer functions (the “tipper”) were estimated by means of the remote reference technique (Gamble et al., 1979) applied to the robust processing method of Sutarno (2008). When necessary, a coherence rejection scheme (Jones

and Jodicke, 1984) was additionally applied. The obtained curves of apparent resistivity and phase resulted of overall very good quality due to the very low noise level affecting the area (see Fig. 7 for an example of apparent resistivity-phase curves at two stations).

In order to assess the electromagnetic dimensionality of the area, we computed the induction arrows (Parkinson, 1959) and the phase tensor ellipses (Caldwell et al., 2004). They are shown in Fig. 6 for the frequencies 82, 0.4, 0.07 and 0.006 Hz together with the phase tensor skew displayed by a colour scale ranging from red (+5) to blue (-5). For frequencies above 0.4 Hz (corresponding to a skin depth of about 3.6 km at $20 \Omega\text{m}$), low ellipticity, skew values and induction arrows magnitudes are observed all across the Luhoi area, attesting a nearly 1D

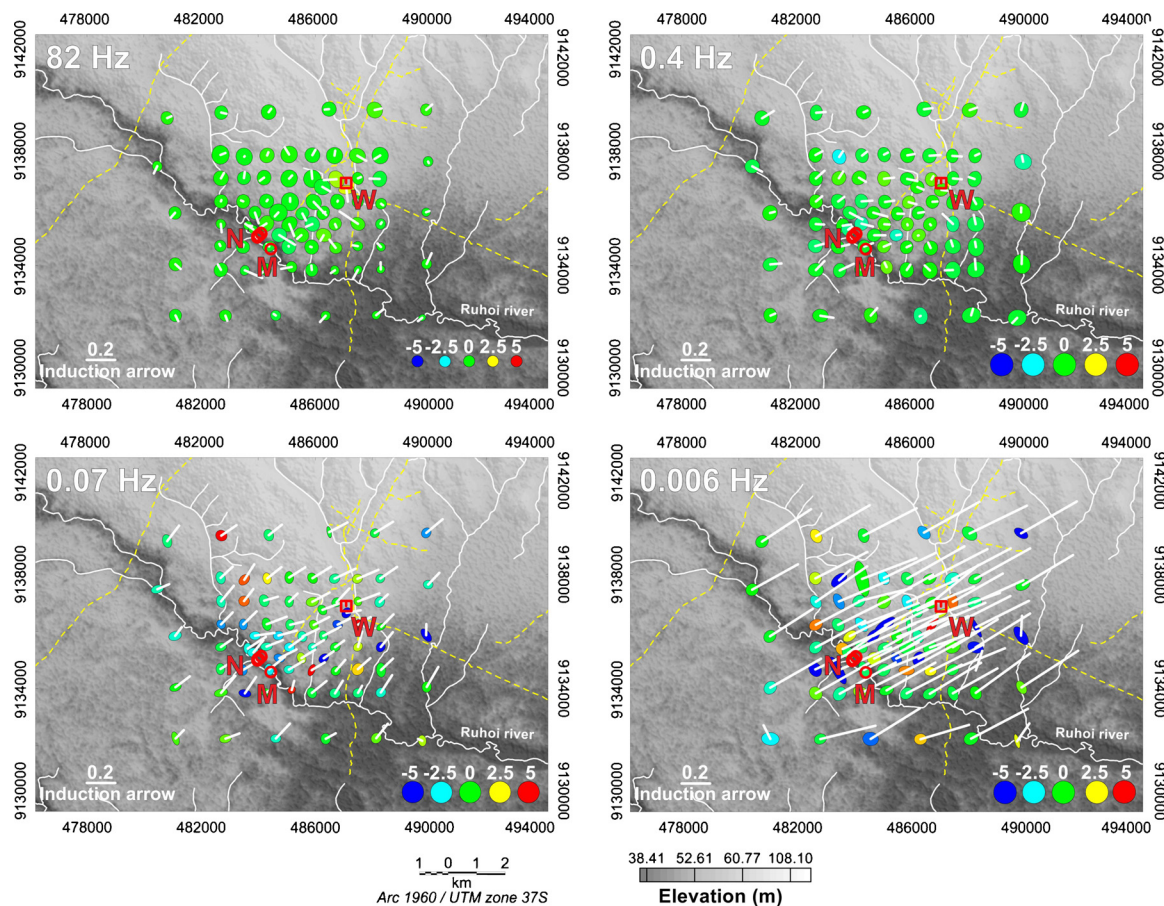


Fig. 6. Induction arrows (Parkinson, 1959), phase tensor ellipses (Caldwell et al., 2004) and phase tensor skew displayed by a color scale ranging from red (-5) to blue (5) for the frequencies 82, 0.4, 0.07 and 0.006 Hz. Induction arrows point towards conductive regions (Parkinson convention). (For interpretation of the references to colour in this figure legend, the reader is referred to the web version of this article).

environment. At lower frequencies, higher dimensionality conditions appear. Note also the progressive magnitude increase and alignment of the induction arrows towards NNE (Parkinson convention) at the lower frequencies due to the sea effect from Indian Ocean located about 60 km to the East of the study area. This effect has been modelled and incorporated in the 3D MT inversion model shown in Fig. 8.

One of the major effects of galvanic distortion on MT data is the frequency-independent ("static") vertical shift that affects the apparent resistivity leaving the MT phase nearly undistorted (Sternberg et al., 1988; Ogawa, 2002). This phenomenon can also be caused by a rough topography or strong lateral resistivity contrasts (Jiracek, 1990; Ogawa,

2002), but these factors were not expected to be important in the Luhui basin since the flat topography and the expected low resistivity contrasts inferred from the resistivity log at Ruaruke North 1 well (see Fig. 2). To estimate the static shift affecting MT data, we used Time Domain ElectroMagnetic (TDEM) measurements collected at the same MT locations by means of square 100 or 200 m transmitter loops and obtaining acceptable data up to about 70 ms and more. Following the approach proposed by Meju (1996), the MT phase and TDEM data (both not affected by the static shift) have been jointly inverted to retrieve a 1D undistorted resistivity model at each site. The computed MT apparent resistivity from the obtained resistivity model has then been

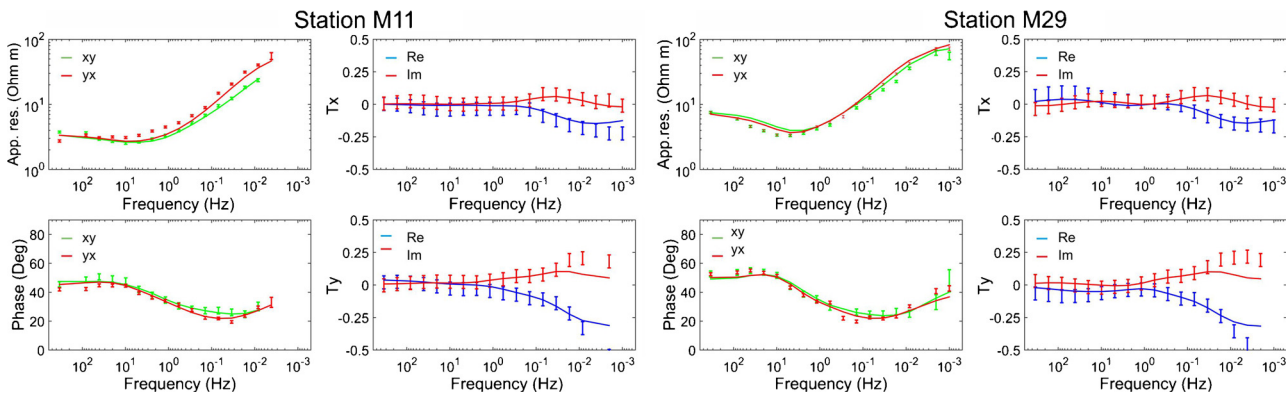


Fig. 7. MT apparent resistivity, phase, and tipper components (Tx, Ty) curves at stations M11 and M29 (see Fig. 4 for location). Error bars: measured data; continuous lines: response of the final 3D resistivity model shown in Fig. 8.

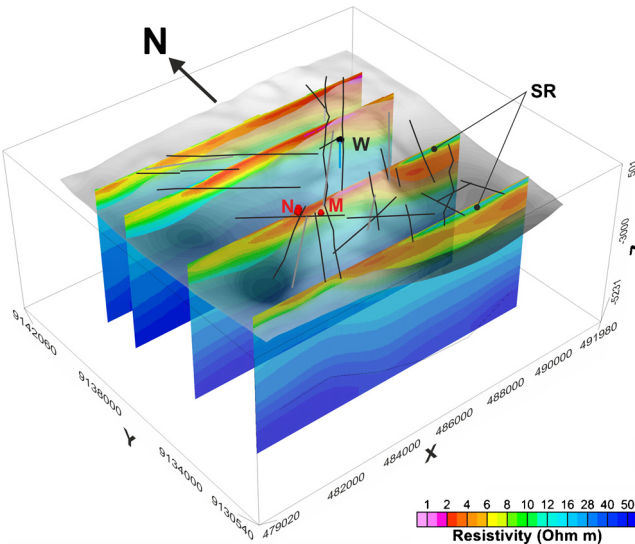
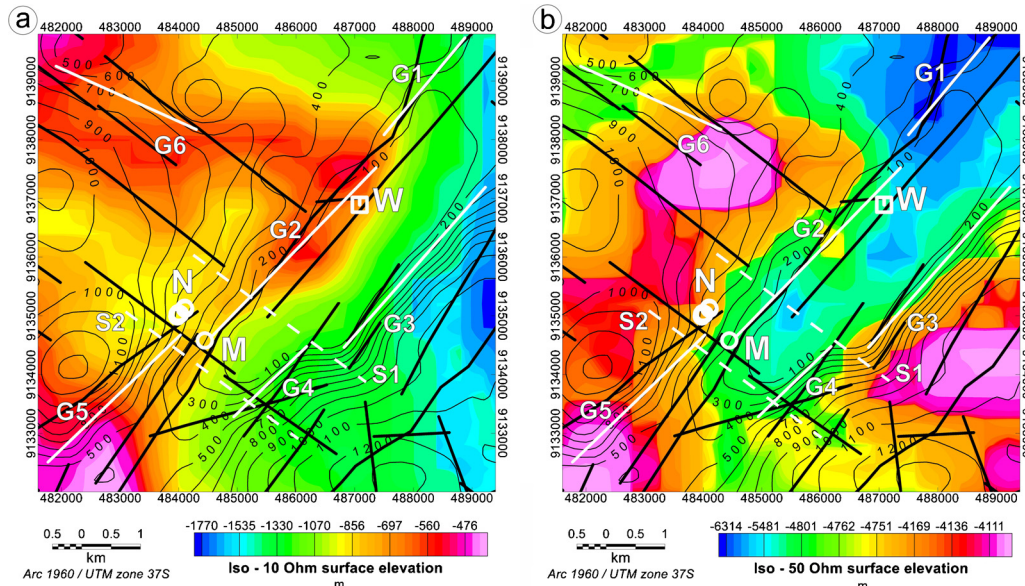


Fig. 8. 3D view of the MT electrical resistivity model through EW sections; the transparent gray surface is the contact surface (with thickness ranging from 0 to 1300 m) between the Ruaruke claystones and the Kipatimu sandstones, imaged by the 3D gravity inversion. Black lines are the major lineaments derived by remote sensing analysis. gGray lines are the gravimetric lineaments traced in Fig. 5. Labels N, M and W indicate the Nyongoni, Mkolwa and Wingoyongo manifestations, respectively. SR: sand lens in the Ruaruke claystones.

used as reference to correct the measured MT apparent resistivity data through a multiplicative shift factor, obtaining a final static shift-free impedance data set.

Three-dimensional inversion of MT data was accomplished by means of the ModEM software described by Egbert and Kelbert (2012) and Kelbert et al. (2014) with additions for parallel computing (Meqbel, 2009). ModEM is based on a finite differences approach to solve Maxwell equations on a staggered grid and operates functional minimization in the data space. The software inversion scheme penalizes model perturbations obtained after each iteration against a prior model, which is coincident with the initial model. The model discretization we have adopted for Luhoi consists of 70×70 cells in North and East directions, extending 250 km far from the survey area. In the survey area the adopted horizontal cell size is 300 m. The Indian Ocean has been included in the model usingETOPO1 (Amante and Eakins, 2009)



bathymetry with 1 arc-minute resolution and assuming for the sea water resistivity of 0.3 Ω m. In the vertical direction, the grid consists of 95 layers, with bottom located at a depth of 683 km. At the shallowest depth, the minimum thickness of each cell is 25 m and then it increases exponentially with depth. Topography from the SRTM digital elevation model (USGS product) has been included in the model. For the final 3D inversion, we used the full (unrotated) and static shift-corrected impedance tensor jointly with the vertical magnetic transfer functions from all the 76 stations, using 37 periods in the range between 0.003 s and 1000s. Some heavily biased or scattered data points were discarded.

The 3D inversion was carried out with different initial models: a model derived from interpolation of smooth 1D models and two half spaces with uniform resistivity of 20 and 50 Ω m. The three different initial models gave very similar results. As preferred final model we choose the one derived from the 1D interpolated initial model because in most of the area dimension analysis suggested a close to 1D resistivity distribution (see Fig. 6). The final normalized RMS was 1.5. As example of data fit, in Fig. 7 we show the response for two stations (M11 and M29).

In Fig. 8 we show the final 3D model by means of four vertical resistivity cross-sections, stacked in a perspective view. We have also reported in gray the sandstone-claystone interface derived from the 3D gravimetric inversion (see Fig. 5b) that images the horst structure. The electrical resistivity model is primarily characterized by a conductive shallow layer (resistivity range 1–10 Ω m) covering all the survey area with thickness ranging from 200 to 1000 m. We have reported in Fig. 9a the iso-resistivity surface at 10 Ω m as representative of the bottom of the conductive layer and compared it with the gravimetric surface as contour lines. Generally, there is a good correspondence between the two surfaces. Moreover, the resistivity range of the conductive layer (1–10 Ω m) is in good agreement with the 2–6 Ω m values directly measured in the Ruaruke claystones by an electrical log at the Ruaruke-North-1 well (derived from the original well log shown in Fig. 2). Therefore, we interpret the conductive layer as the Ruaruke claystones layer. Some discrepancies between the MT and the gravimetric signatures will be discussed in the following paragraph.

In the SE part of the survey area (Fig. 8), a shallow resistive layer labelled SR of about 20 Ω m is visible. This feature likely represents a sandstone intercalation in the Upper Cretaceous claystones. Similar intercalations have been observed in the same formation in the Ruaruke-North-1 well (Fig. 2). The NW edge of the sandstone intercalation SR has the same NE trend of the horst that therefore has likely

Fig. 9. Elevation a.s.l. of the iso-resistivity surfaces from the 3D MT resistivity model at a) 10 Ω m and b) 50 Ω m. Continuous and dashed white lines are the gravimetric lineaments as defined in Fig. 5. Black lines are the lineaments derived from the remote sensing analysis. Labels N, M and W indicate the Nyongoni, Mkolwa and Wingoyongo manifestations, respectively. Contour lines represent the elevation of the gravimetric bedrock.

controlled its deposition, providing a constraint on the horst dating. The horst uplift is obviously younger than the Lower Cretaceous sandstones that forms it and older than the Upper Cretaceous claystones containing the sandy lens whose deposition has been controlled by the horst itself. However, reactivation in more recent time is plausible and could provide secondary porosity not still heavily reduced by self-sealing.

At depth, the MT resistivity iso-surfaces show a down-dome in correspondence of the detected horst structure. As example, we show the 50 Ωm iso-surface (Fig. 9b) that presents an opposite signature with respect to the up-dome shown at shallow depth by the 10 Ωm iso-surface (Fig. 9a). This indicates that lithology does not have control on the resistivity distribution at depth. On the contrary, electrical conductivity is likely enhanced at depth by secondary porosity due to faulting and fractures and possible clay alteration. This deep resistivity signature implies that faulting generating the horst is pervasive and likely reaches the basement. Note that at depth greater than 5 km (not shown in Fig. 8) the 3D resistivity model does not reveal any conductor to be associated with any localized deep heat source that could explain the Luhoi thermal anomaly. Also note that recent interpretations of deep resistive anomalies (30–50 Ωm) as partial melt in the hydrothermal system of Newberry Volcano (Bowles-Martinez and Schultz, 2020) appear here very unlikely due to the lack of geochemical evidence of magmatic activity and the low temperatures estimated by water geothermometers.

Resistivity of the final 3D model (Fig. 8) smoothly increases with depth without showing sharp vertical resistivity variations that might be associated to lithological contrasts. This effect can derive from the smooth regularization functional adopted by the inversion algorithm in ModEM. To investigate the possible presence of lithological interfaces with high expected resistivity contrasts (see Fig. 2), we therefore used MT 1D blocky inversion and sensitivity testing by forward 1D modelling along the profile shown in Fig. 10 and located in Fig. 4. The profile location has been chosen in order to consider only stations with an approximatively 1D resistivity distribution as shown by the phase tensor ellipses and skew (see Fig. 6) and therefore excluding the central horst area from this analysis because of the expected strong 3D effects (Fig. 9b). First, we tested the possible presence at Luhoi, beneath the Kipatimu sandstones, of the claystones of the Bagamoyo Formation (as found at the Kisangire-1 well, see Fig. 2), assuming for them a resistivity of 1–6 Ωm , that is the same order of the resistivity measured in the younger Ruaruke claystones. Sensitivity tests show that such a conductive layer at depth should be easily seen in the MT data and therefore we can exclude its presence in the Luhoi area. We conclude that at Luhoi the Middle Jurassic Pindiro limestones directly underlie the Kipatimu sandstones, similarly to the Lukuliro-1 well (Fig. 2). The 1D MT sensitivity analysis indicates that the Pindiro limestone resistivity (8–50 Ωm) lies in the same range of the Kipatimu sandstones

(10–30 Ωm) and therefore the interface between the two formations cannot be detected. Its depth (dashed black line in Fig. 10) has been estimated to be of the order of 2–2.5 km below the surface assuming a Kipatimu sandstones maximum thickness of 1–1.5 km on the base of the Kisangire-1 well evidence and the global estimations in the Tanzanian coastal basin (e.g. Said et al., 2015). Below the Middle Jurassic Pindiro limestone layer, blocky 1D inversion models at all MT stations show a resistivity bedrock (Fig. 10) at 3–5 km depth with resistivity in the range 40–160 Ωm . The estimated depth is comparable with the Karoo sandstones depth found in the Kisangire-1 well (about 2 km), considering the additional thickness of about 1 km of the overlaying Ruaruke claystones in Luhoi.

Beneath the Karoo formation, we didn't find any evidence in the MT 1D blocky models of the Precambrian gneiss basement. Sensitivity test indicates a possible resistivity range of 40–160 Ωm comparable with the overlying Karoo formation.

4.3. Magnetic survey

In order to check the presence of buried dykes and other volcanic features, we carried out a detailed ground magnetic survey over the study area by a proton processing magnetometer along 16 lines with a nominal separation of 300 m and four tie lines. The mean point separation along each line was 9.8 m giving 7951 measurements and a total length of the lines of 77 km. After temporal correction, levelling procedures and IGRF field removal, the residual magnetic anomaly map (not shown) does not exhibit any clear interpretable pattern associated with any geological source. The high wave-number and low intensity detected signal is ascribed to lateral susceptibility variations in the soil that were not attenuated by the 2.5 m high pod used to host the sensor. The lack of magnetic signatures supports the hypothesis of absence of volcanic features, contrary to the first interpretations of Luhoi as a volcanic geothermal field with an intermediate depth reservoir presumably hosted in volcanic rocks (Kent et al., 1971; Jica, 2014).

5. Discussion

Hereafter we discuss the main constraints on the Luhoi geothermal conceptual model derived from the geophysical investigations.

5.1. Shallow structure

We have interpreted the main gravimetric anomaly (Fig. 5a) as the signature of the lateral density contrast between the Kipatimu sandstones and the Ruaruke claystones generated by the normal fault system associated to the detected local horst structure (Fig. 5b). To get a more realistic image of the horst, in Fig. 11b we have refined the density

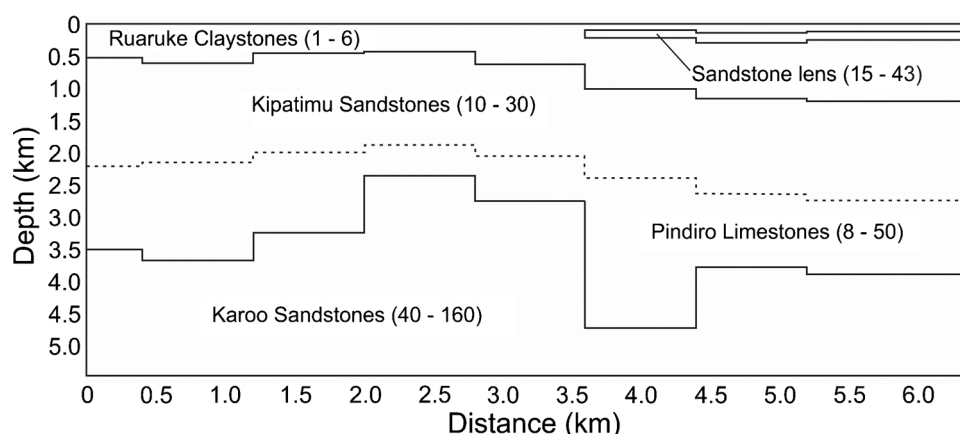


Fig. 10. Resistivity pseudo-section made by interpolation of MT 1D blocky models. The section is located in Fig. 4. The resistivity range for each layer is reported in Ωm . The dashed interface between the Kipatimu sandstones and the Pindiro limestones is inferred from mean thickness of the former one reported in the literature.

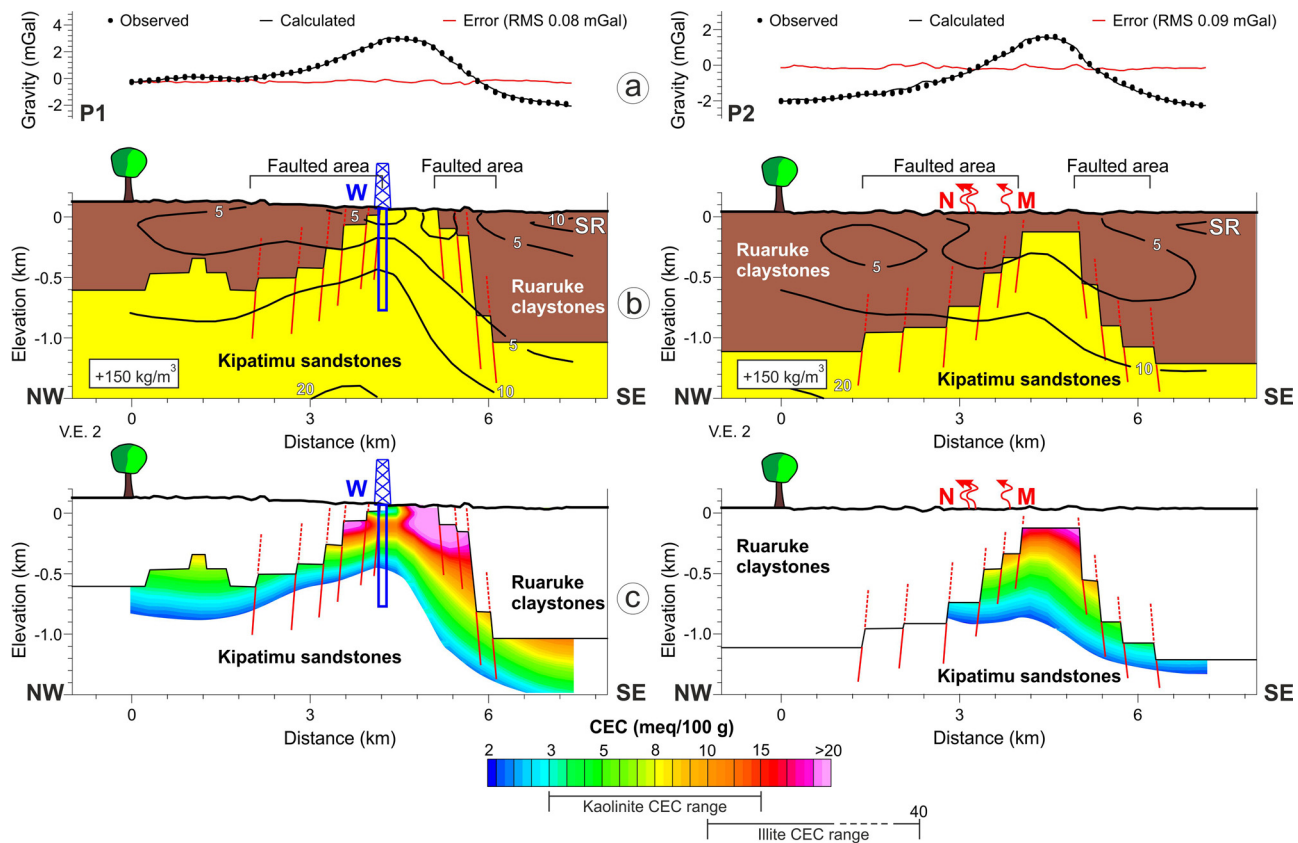


Fig. 11. a) Gravimetric residual Bouguer anomaly along sections P1 and P2 localized in Fig. 4 and 5. b) Ruaruke claystones – Kipatimu sandstones contact surface imaged by 2D gravimetric forward models; we have modified the surface derived from 3D inversion (Fig. 5b) to better simulate a horst structure with close to horizontal/vertical interfaces; the density contrast is 150 kg/m^3 ; 3D MT electrical resistivity contour lines (Ωm) have been superimposed on the models; inferred faults are reported as red lines; SR: sandstone lens; N, M, W: Nyongoni, Mkolwa and Wingoyongo manifestations. c) Distribution of the cation exchange capacity (CEC) of clay in the Kipatimu sandstones derived from the 3D MT electrical resistivity by the Waxman and Smits (1968) formula. (For interpretation of the references to colour in this figure legend, the reader is referred to the web version of this article).

contrast interface derived from 3D inversion by 2D forward modelling allowing only for roughly horizontal and vertical segments that simulate normal fault scarps. The two models are orthogonal to the main NE trending gravimetric anomaly and cross the Wingoyongo hill (P1) and the Nyongoni/Mkolwa springs (P2). The final picture (Fig. 11b) images an asymmetric horst structure with up to 1 km of vertical displacement. Asymmetry of the horst may control the preferential up-flow path of the geothermal system. The models show that the down-throw of the NW flank of the horst is originated by a set of normal faults distributed over a length of about 3 km covered by a thinner (with respect to the SE side) claystone layer. All the manifestations (Nyongoni, Mkolwa and Wingoyongo) occur along this flank of the horst. Moreover, the hot springs at Nyongoni are aligned along this feature (dashed black line ST1 in Fig. 4). At the SE flank of the horst, the larger down-throw displacement is due to a few faults concentrated over a shorter length (about 1 km) and covered by a thicker claystone layer that likely hampers the propagation of the fluids up to the surface.

Geophysical models, gravity trend analysis and remote sensing lineaments have imaged two structural trends affecting the study area: NE and NW to WNW. The NE structural trend is associated to the imaged NE trending horst structure. This trend is compatible with the regional Tanga trend enlightened by the regional structural map (Fig. 1a) and regional potential field data interpretation (Fig. 3). The NW to WNW trend is evident in remote sensing lineaments and is visible as secondary lineaments in both gravimetric (Fig. 5) and magnetotelluric models (Fig. 9). It can be related to the regional Manzini–Tagalala trend or to the Rufiji Trough trend. Note that the Nyongoni springs group and the Mkolwa spring are aligned along this

trend (dashed black line ST2 in Fig. 4) at the intersection with the NW flank of the horst. A higher permeability is expected at the intersection of the two fault systems.

Note that there is no clear electrical resistivity signature in the 3D model directly associated with the normal faults system inferred from the gravity analysis, as detected in some other similar systems. For instance, in the Chingshui geothermal field (Chang et al., 2014) located in the Ilan Plain (Northeast Taiwan) and connected to the Okinawa Trough back arc basin, the main fault systems are associated with conductive anomalies and high temperatures ($> 140^\circ\text{C}$) revealed by core logs. On the contrary, the faults signature in the MT resistivity model here is more reminiscent of the signatures obtained for instance in the geothermal systems along the Kenya rift by Lichoro et al. (2017, 2019), in the Mbaka system (Rizzello et al., 2018) in southern Tanzania or at Alalobeda in northern Ethiopia (Rizzello et al., 2016), where faults are revealed in the resistivity MT models by vertical shifts of the bottom of the shallower conductive layers (usually associated with low temperature clay alterations) and confirmed by the gravimetric signatures.

5.2. Clay cap

In Fig. 11b we have superimposed the resistivity contours derived from the MT 3D model on the gravimetric 2D models. In both sections, the sandstones horst apex shows anomalous low resistivities ($< 5 \Omega\text{m}$) that are similar to the values found in the adjacent claystones. In the Wingoyongo-1 well (Fig. 2) traces of hydrothermal alteration were found below 44.5 m depth and kaolinitic sandstones occurred from 112 to 395 m (Kent et al., 1971). Therefore, low resistivity may be used as a

proxy to map the clay content in the shallower portion of the sandstone horst. To be more quantitative, we have first estimated the formation factor F of the sandstones at Wingoyongo-1 below 500 m, where no significant clay content is reported in the well log, and consequently nearly pure electrolytic conductivity is expected. The formation factor F is defined in the first Archie's equation (e.g. Schön, 1996) as the ratio between the bulk ρ and the pore fluid ρ_w resistivities and it is related to the porosity Φ via the cementation factor m and an empirical parameter a :

$$F = \frac{\rho}{\rho_w} = \frac{a}{\Phi^m}$$

The mean bulk resistivity in the depth range 500–2000 m from the MT 3D model at Wingoyongo (Fig. 11a) is $\rho = 16.3 \Omega \text{ m}$. Resistivity of the saline geothermal water was measured at the Nyongoni springs and resulted $\rho_w = 0.9 \Omega \text{ m}$. The resultant formation factor is $F = 18.1$ and the correspondent cementation factor, for a mean porosity $\Phi = 18 \%$ (derived from well data) and assuming $a = 0.6$ (suggested value for moderately well cemented sedimentary rocks by Keller, 1989), is $m = 2.0$. In order to take into account (possible hydrothermal) clay minerals that reduce sandstone resistivity in the shallower part of the horst, we have applied the Waxman and Smits (1968) formula that extends the first Archie law linking the bulk resistivity to the cation exchange capacity (CEC) of clay, the resistivity ρ_w of the fluid in the pores, the porosity Φ and the formation factor F ; F is assumed to remain the same as in the pure electrolytic conduction case. Re-arranging the original formula, the CEC value is given by:

$$\text{CEC}(\rho) = \left(\frac{\rho_w \cdot F - \rho}{\rho_w \cdot \rho} \right) \cdot \frac{\Phi}{1-\Phi} \cdot \frac{100}{B \cdot d}$$

where

$$B = 3.83 \cdot [1 - 0.83 \cdot e^{(-0.5/\rho_w)}]$$

and d is the grain solid density (Schön, 1996).

The result obtained at Wingoyongo is shown in the graph of Fig. 12. The estimated CEC values are compatible with those expected for kaolinite (range 3–15 meq/100 g, mean value 10 meq/100 g, Grim,

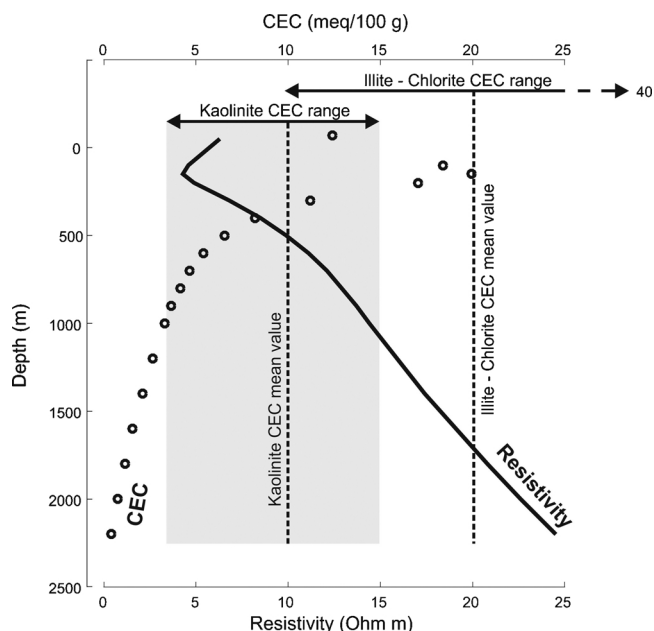


Fig. 12. Relationship between 3D MT electrical resistivity and the cation exchange capacity (CEC) of clay in the Kipatimu sandstones at Wingoyongo. CEC of clay has been computed by the Waxman and Smits (1968) formula from the 3D MT electrical resistivity. Most of the estimated CEC values are in the kaolinite range and partially in the illite/chlorite range (Ussher et al., 2000).

1953); other clay minerals with CEC up to 20 meq/100 g may be present such as chlorite and illite (range 10–40 meq/100 g, mean value 20 meq/100 g). Kaolinite is one of the most common eogenetic clay minerals in sandstones (e.g. Worden and Morad, 2003) and usually derives from feldspar alteration due to fluids rich in CO_2 and/or organic acids (likely occurring at Wingoyongo) and/or meteoric fluids (Lanson et al., 2002). Illite is expected to derive from kaolinite at temperatures greater than 70–90 °C (Worden and Morad, 2003) and may be present here; however, since complete illitization of kaolinite in sandstones is expected to occur at about 130 °C (Worden and Morad, 2003), the estimated CEC values lower than 10 meq/100 g and the observed kaolinite sandstones in Wingoyongo-1 well would imply that temperatures never reached these values. Chloritization of kaolinite has been reported for instance in the upper Cenozoic sediments in the Salton Sea geothermal field and the Salton Trough at temperatures not lower than 180 °C (Muffler and White, 1969) and therefore it is unlikely here, considering that Luhui expected reservoir temperature is close to 100 °C based on water geothermometers.

The CEC distribution can be derived from the 3D electrical resistivity distribution along the whole horst sector and used as a proxy for pervasive presence of clay minerals as shown in Fig. 11c. All the shallower portion of the Kipatimu sandstone horst results affected by a higher clay content that likely reduces its porosity and permeability. Note that the shallow clay rich layer is thicker in the SE sector of the horst where it reaches a depth of the order of 1500 m. This shallow clay rich layer affecting the horst together with the Ruaruke claystones layer forms a continuous medium acting as a typical clay cap and limiting the up-flow of hot water from the Kipatimu sandstones.

However, our interpretation of the shallow low resistivity signature in the sandstone horst imaged at Luhui is different from the typical resistivity pattern of high-temperature geothermal systems in volcanic environment (e.g. Cumming, 2009; Cumming and Mackie, 2010; Árnason et al., 2010; Múnoz, 2014). In such high-temperature systems the typical shallow low resistivity layer corresponds to the clay cap made by low temperature and low resistivity smectites with very high CEC values (e.g. Ussher et al., 2000; Lévy et al., 2018); below the clay cap, higher temperature stable illite and chlorite are expected to increase the resistivity due to their lower CEC. This transition depends on temperature (about 200 °C, Ussher et al., 2000) and therefore the iso-resistivity contours may represent a proxy for the isotherms (e.g. Lévy et al., 2018). At Luhui, the typical low resistivity clay minerals in the cap-rock of high-temperature geothermal systems, smectites, are unlikely because of their typical CEC range (80–150 meq/100 g; Grim, 1953) much higher than the estimated ones (< 30 meq/100 g). The low resistivity (< 5 Ωm) signature of the shallow sector of the sandstone horst is therefore due to low CEC clays coupled with highly conductive (0.9 Ωm) fluids. Significant contribution of very high salinity fluid to the bulk clay cap resistivity has been also reported for instance by Flóvenz et al. (2005) and Lévy et al. (2018) as particular cases in some basaltic rocks in high enthalpy systems. The low resistivity pattern here is similar to the one detected for instance in the shallower portion of the low enthalpy Groß Schönebeck geothermal site in the Northeast German Basin where the shallowest (< 2 km depth) high-conductivity anomalies image alternating sequences of clay-rich formations and weakly consolidated sandstones of Cretaceous to Upper Triassic age (Múnoz et al., 2010a, 2010b). On the contrary, at the low enthalpy Skierniewice geothermal test site (Poland), the shallow zones of lower resistivity indicate highly porous and/or fractured zones rather than eogenetic clay rich layers (Bujakowski et al., 2010).

Moreover, at depth, the expected maximum temperature of the reservoir (close to 100 °C) does not allow a pervasive transformation of the low temperature clays into more resistive high temperature clays as in typical high enthalpy geothermal systems. The increase of resistivity with depth in the Luhui sandstones is therefore likely due to the reduction of the alteration clay content with depth. This may be due to unfavorable pH conditions and/or insufficient availability of alkaline

and alkaline-earth cations necessary to form illites and smectites (Grim, 1953).

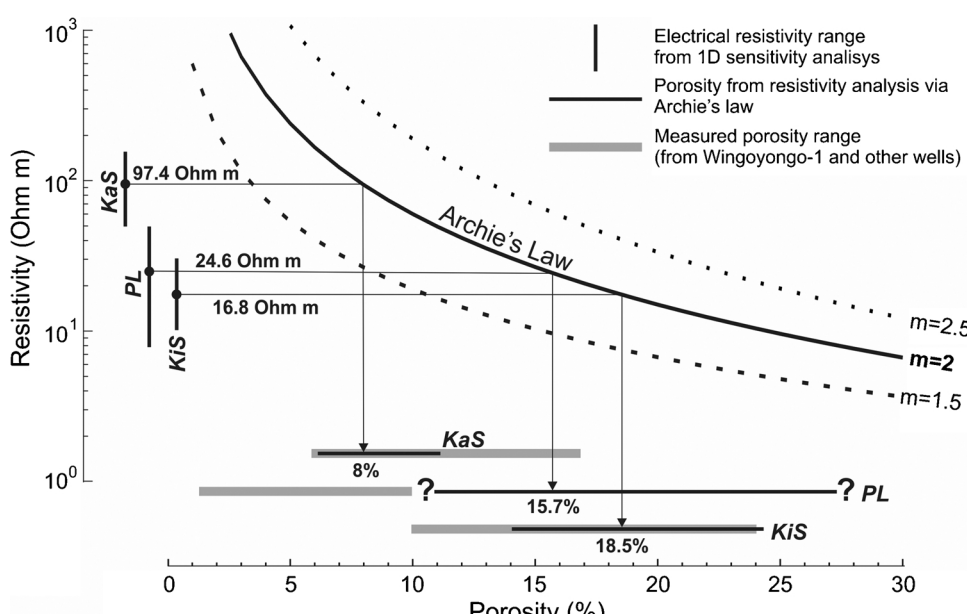
5.3. Deep stratigraphy and porosity

The deep stratigraphy below the Kipatimu sandstones has been inferred from the MT 1D blocky models (see paragraph 4.2 and Fig. 10) constrained by the stratigraphic correlations with the closest wells shown in Fig. 2. The presence of the Bagamoyo claystones beneath the Kipatimu sandstones has been excluded at Luhoi by 1D MT sensitivity tests. The stratigraphic column below the sandstones is therefore composed (see Fig. 10) by the Pindiro limestones (resistivity range 8–33 Ωm), the Karoo sandstones (40–160 Ωm) and the Precambrian gneissic basement (40–160 Ωm). Note that the resistivity values of both the Karoo sandstones and the Precambrian gneissic basement are lower than the values recorded in the same formations in Malawi (unpublished data) and in the Southwest of Tanzania (Rizzello et al., 2018). The lower resistivity values here may be explained by the higher salinity of pore fluids and/or, in the Karoo, by a higher percentage of the fine-grained component.

Inferences on the porosities of the stratigraphic units below the bottom hole of Wingoyongo-1 can be obtained from the log measurements in the same formations at the close by wells (Fig. 2). Independently, they may be estimated via Archie's law (e.g. Schön, 1996), in the assumption of negligible clay content, considering the bulk resistivity ranges inferred from the MT 1D sensitivity analysis and assuming tentatively for all the formations the parameters estimated for the Kipatimu sandstones: cementation exponent $m = 2$ (see paragraph 5.2), $a = 0.6$ (Keller, 1989) and resistivity of the saline geothermal water $\rho_w = 0.9 \Omega\text{m}$.

$$\Phi = (\rho / (\rho_w \cdot a))^{-(1/m)}$$

The comparison between expected porosities from Archie's law and the measured porosities at the nearby wells allows to verify whether a pure electrolytic conductivity in the pore brines may justify the measured resistivities or enhanced conductivity due to clays (possibly derived from hydrothermal alteration) must be invoked. Estimated resistivities from the MT 1D sensitivity analysis, predicted porosities via Archie's law and measured porosities in the close wells for the different stratigraphic units are compared in Fig. 13.



KaS: Karoo Sandstones PL: Pindiro Limestones KiS: Kipatimu Sandstones

The Kipatimu sandstones show a resistivity in the range 10–30 Ωm (excluding the shallow clay rich layer, see paragraph 5.2) which provides a mean porosity of 20 % according to Archie's formula. This value is within the measured range at the Wingoyongo-1 (10–21 %) and at Lukuliro-1 (15–24 %) wells. The resistivity range of the Middle Jurassic Pindiro limestones is 8–33 Ohm m, and the resulting mean porosity according to Archie's law is 18 %. The measured porosity of the Lukuliro-1 Pindiro limestones (4–10 %) is significantly lower than the estimated value at Luhoi in the assumption of pure electrolytic conductivity in the pore brines. This inconsistency may indicate that i) wrong m and a parameters have been adopted for the limestones and/or ii) eogenetic/mesogenic clays are present lowering the resistivity. In the second case, the porosity of the Pindiro limestones could be also lower than at Lukuliro-1. The same approach leads to estimate a mean porosity of about 8 % for the Karoo sandstones that shows a resistivity range between 40 and 160 Ωm. The inferred porosity is in agreement with the Lukuliro-1 and Kisangire-1 well measurements. Analogous low porosity has been obtained for the Precambrian Gneiss Basement.

5.4. Regional circulation and recharge area

On the base of isotope vs. elevation relations (derived from the long-term weighted average oxygen-18 and deuterium values of the Dar es Salaam WMO-IAEA station and assuming isotopic lapse rates of -0.2‰/100 m for oxygen-18 and -1.6‰/100 m for deuterium (Clark and Fritz, 1997), we have estimated the average infiltration elevation of meteoric waters feeding the Luhoi geothermal system to be between 470 and 830 m a.s.l.. Although these results have to be considered educated guesses due to the approximated approach adopted to obtain the isotope - elevation relations, they suggest that the recharge area of the Luhoi geothermal circuit is situated at large distance.

Moreover, the high measured 40Ar/36Ar isotopic ratio (Kraml et al., 2014) suggests that circulation occurs, at least partly, in rocks relatively rich in K-bearing minerals, such as the Precambrian Gneiss Basement and/or the Karoo sandstones deriving from the basement dismantle. On this base, two not mutually exclusive different alternatives are possible for the recharge area location. Meteoric water may infiltrate East of Ulugulu Mountains (Fig. 1a and c) along the Tanga Fault Zone (Kraml et al., 2014), move at depth through the Karoo sandstones and the basement and then, upon heating, flows up and

Fig. 13. Porosity ranges estimated via Archie's law (e.g. Schön, 1996) from the resistivity ranges derived by 1D sensitivity tests, on the assumption of dominant electrolytic conduction in the pore brines. In the Archie's law we have adopted the following values: cementation exponent $m = 2$, $a = 0.6$ (Keller, 1989) and resistivity of the saline geothermal water $\rho_w = 0.9 \Omega\text{m}$. Archie's law curves with $m = 1.5$ and $m = 2.5$ are also shown for comparison (dashed and dotted lines). The estimated porosity ranges (horizontal black lines) are compared with the measured porosities (horizontal gray lines) at Wingoyongo and the other wells shown in Fig. 2. Note the mismatch for the Pindiro limestones indicative of wrong Archie's law parameters and/or enhanced conduction in the limestones due to the cation exchange capacity of clay.

moves through the Kipatimu sandstones. The Maminzi-Tagalala and the Rufiji structural trends (Fig. 1a) may act as preferential pathway. Alternatively, meteoric water may infiltrate in the Mt. Matumbi area, to the South of Luhoi, and move towards Luhoi eventually along preferential enhanced porosity pathway given by the NW trending Tanga structural trend lineaments.

5.5. Heat source

Regional potential field analysis coupled with the geochemical evidence (see paragraph 3) and the detailed ground magnetic survey (paragraph 4.3) have excluded the presence of volcanic or plutonic active heat sources. This is also confirmed by the lack of deep conductors in the 3D resistivity model (Fig. 8) also at depth greater than 5 km. Enhanced geothermal gradients at Luhoi may therefore be explained by two other main different causes.

Geothermal systems heated by crustal thinning with consequent asthenosphere upwelling (extensional type play of Moeck, 2014) are typical of tectonically active intra-continental rift grabens such as the Tendaho Graben in the northern East African rift where the Dubti, Ayrobera (Stimac et al., 2014; Armadillo et al., 2016) and Alalobeda (Rizzello et al., 2016) geothermal systems are found. In these systems, upflow of geothermal fluids is controlled by faulting (Battistelli et al., 2002; Didana et al., 2015; Pasqua et al., 2016) similarly, for instance, to the geothermal systems in the Great Basin in western U.S. (McKenna and Blackwell, 2004; Faulds et al., 2010), in Western Turkey (Faulds et al., 2009) and in the Upper Rhine Graben (Freymark et al., 2017). Additionally, radiogenic heat production from the gneiss basement may be considered as possible cause of the enhanced geothermal gradient at Luhoi, similarly to the high radiogenic heat production of the basement made by gneiss and granites in the SW Germany and NE France sector of the Rhine Graben (Freymark et al., 2017).

Alternatively, the Luhoi geothermal system may be reminiscent of an intracratonic basin (intracratonic basin play of Moeck, 2014). In such an environment, both large scale depth variations of the thermal lithosphere-asthenosphere boundary and the insulating effect of thick sediments usually affect the regional geothermal gradient, while local patterns are controlled by the contrasting thermal properties of the different sedimentary lithologies (e.g. Scheck-Wenderotha and Maystrenko, 2013). For instance, in the Paris Basin (Bonté et al., 2010) higher regional geothermal gradients have been observed where the sediments are thicker, suggesting a sedimentary cover insulating effect. On the contrary, the enhanced positive local thermal anomalies in some areas of the Central European Basin System have been related to the heat transport through highly conductive salt layers in contrast with the surrounding low-conductive clastic sediments (Scheck-Wenderotha and Maystrenko, 2013).

Luhoi is located along the proposed continuation of the eastern branch of the EARS from the Northern Tanzania Divergence Zone to a N–S zone of seismicity offshore southern Tanzania and Mozambique (O'Donnell et al., 2013; Mulibbo and Nyblade, 2016). The rift continuation is well visible in the dilatation map of the Sub-Saharan Africa Geodetic Strain Rate Model tensor (Stamps et al., 2018). Dilatation is defined as the trace of the strain rate tensor and its pattern in the Luhoi area (Fig. 14) is indicative of dominantly tensional strain increasing towards East. This trend is correlated with the available geothermal gradient measurements at the Lukuliro-1 ($26.7^{\circ}\text{C}/\text{km}$), Kisangire-1 ($31.5^{\circ}\text{C}/\text{km}$) and Ruaruke-North-1 ($58.5^{\circ}\text{C}/\text{km}$) wells that increase towards the coast (Fig. 14). We therefore interpret the tensional strain pattern as indicative of crustal thinning with consequent increase of the geothermal regional gradient in a tectonically active intra-continental rift, suggesting an extensional type play (Moeck, 2014). However, the estimated Luhoi reservoir temperatures (close to 100°C from water geothermometers according to our estimation, 133°C according to Kraml et al., 2014) are more typical of intracratonic basins like the Paris Basin where temperatures up to 120°C have been recorded in the

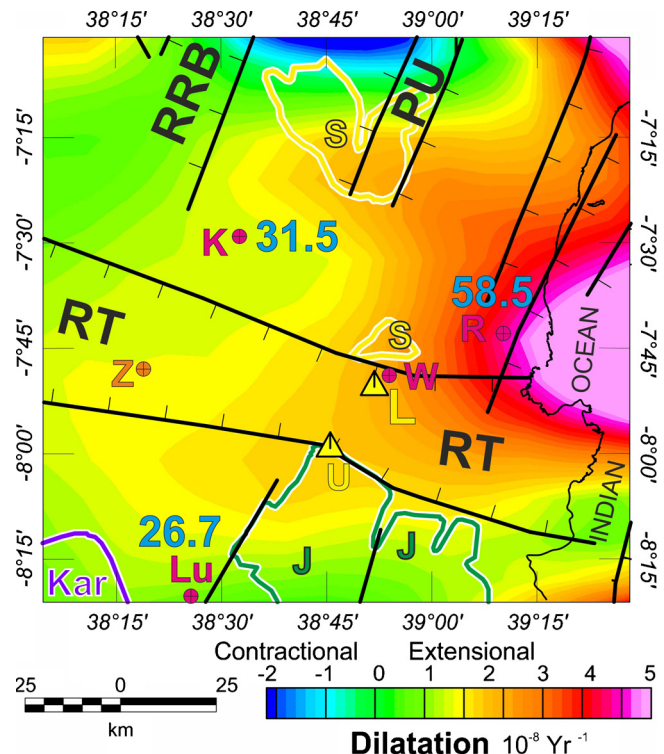


Fig. 14. Dilatation (trace of the tensor) of the Sub-Saharan Africa Geodetic Strain Rate Model tensor by Stamps et al. (2018). Positive dilatation is indicative of dominantly tensional strain, while negative dilatation is indicative of compressional strain. Geothermal gradients derived from the bottom hole temperatures are reported in cyan close to each well (in $^{\circ}\text{C}/\text{km}$). Linear interpolation between geothermal gradients and dilatations at the wells gives an estimation of the geothermal gradient in the Luhoi region of $41^{\circ}\text{C}/\text{km}$. L: Luhoi, U: Utete, Z: Zombe; RRB: Ruvu Rift Basin, RT: Rufiji Trough, PU: Pugu uplift; K: Kisangire-1, Lu: Lukuliro-1, R: Ruaruke-North-1, W: Wingoyongo-1; J: Jurassic sediments, Kar: Karoo sandstones, S: Kipatimu sandstones.

central area at 3000 m depth (Bonté et al., 2010) or back-arc basin like the Pannonian Basin where anomalous heat flow is related to crustal thinning giving anomalous gradients of about 40 – $50^{\circ}\text{C}/\text{km}$ with water temperature in the porous formations reaching 130 – 150°C (Szanyi and Kovács, 2010; Horváth et al., 2015). Note that past higher temperatures than present day ones, possibly suggesting a different heating mechanism active in the past like a pluton source, are unlikely at Luhoi: the preserved kaolinite sandstones observed in Wingoyongo-1 well and the estimated low CEC values indicate not complete illitization of kaolinite that would require higher temperatures; moreover, high temperature alteration is usually unaffected by subsequent cooling and, therefore, its resistivity signature would be preserved (e.g. Árnason et al., 2010; Muñoz, 2014), that is not the case here. Note also that present-day positive dilatation in Luhoi area (Stamps et al., 2018) implies active tensional tectonics and possible consequent reactivation of the Cretaceous Luhoi horst normal faults increasing secondary permeability for fracturing.

5.6. Geothermal gradient estimation and hydrothermal reservoir depth

Assuming a linear relationship between dilatation of the Sub-Saharan Africa Geodetic Strain Rate Model tensor (Stamps et al., 2018) and the known geothermal gradients at the Lukuliro-1, Kisangire-1 and Ruaruke-North-1 wells (Fig. 14), we have obtained an estimation of $41^{\circ}\text{C}/\text{km}$ for the regional geothermal gradient expected in the Luhoi area. The resulting regional isotherms have been drawn in the section of Fig. 15a (away from the horst) and the corresponding reference regional depth-temperature curve is shown as light gray line in Fig. 15b,

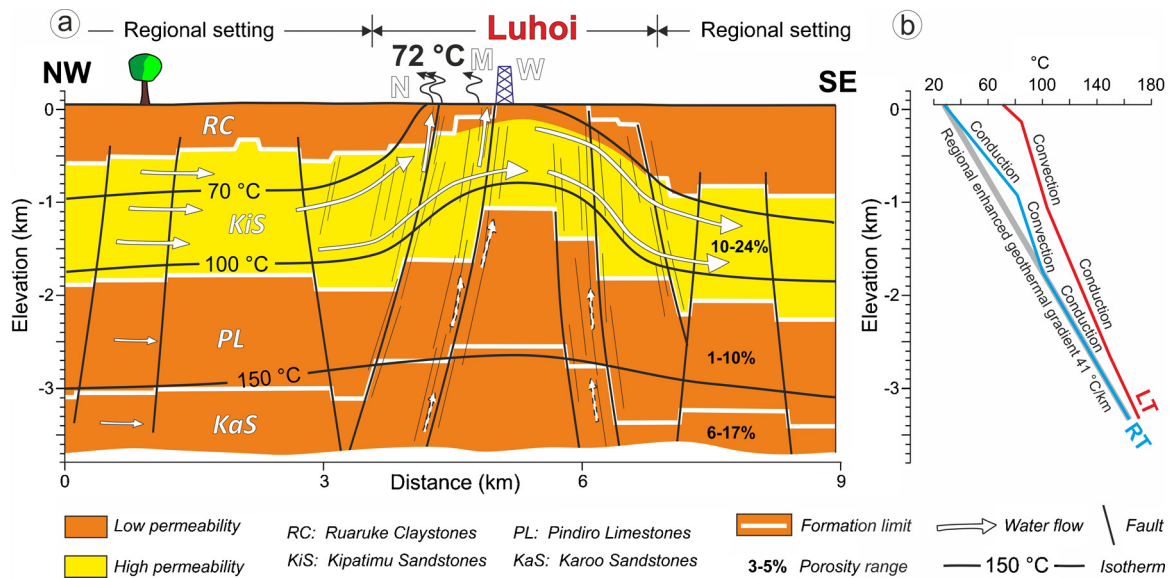


Fig. 15. Conceptual model (e.g. Cumming, 2009) of the Luhoi geothermal system. a) Idealized NW-SE section showing the high permeable Kipatimu sandstones (light grey) sandwiched between low permeability formations (dark grey); the Kipatimu sandstones host the regional reservoir; the horst structure at Luhoi pushes up the sandstones and consequently the regional water flux and the isotherms. b) Qualitative sketch of the expected temperature-depth relationships; light gray line: temperature-depth curve with constant geothermal gradient of 41 °C/km; blue line (labelled RT): regional perturbations due to convective phenomena and lithological thermal conductivity variations; red line (LT): local perturbations at Luhoi due to the horst uplift. (For interpretation of the references to colour in this figure legend, the reader is referred to the web version of this article).

in the assumption of homogeneous thermal conductivity and no convection. At a regional scale, this ideal behavior is perturbed by the different thermal conductivity between the lithological formations and by the convection affecting the Kipatimu sandstones revealed by temperature-depth curves in the nearby wells (Fig. 2). As qualitative example, a possible resultant regional temperature-depth curve is shown in the sketch of Fig. 15b as blue line labelled RT.

Considering the 41 °C/km regional geothermal gradient and that our most reasonable estimate of the Luhoi reservoir temperature is close to 100 °C, reservoir depth in the region outside Luhoi can be estimated to be in the order of 1.7 km (assuming a mean surface temperature of 25 °C). In the case of the reservoir temperature estimation of 133 °C by Kraml et al. (2014), the estimated depth is 2.6 km. The resultant depth range (1.7–2.6 km) has the same order of magnitude of the expected depth of the Kipatimu sandstones - Pindiro limestones interface (Fig. 10) outside the horst area. We conclude therefore that the geothermal reservoir is likely hosted in the permeable Kipatimu sandstones.

At Luhoi, a strong local perturbation is expected, due to the horst structure moving the Kipatimu sandstone layer to the surface. As result, the local gradient is strongly enhanced at shallow depth (red curve LT in the sketch of Fig. 15b) giving a correspondent up-dome of the isotherms (Fig. 15a). Consequently, the estimated depth of the geothermal reservoir at Luhoi is of the order of 500 m and its thickness of the order of 1 km.

Minor contributions to the geothermal system from deeper waters are expected through the deep faults affecting the limestones, the Karoo sandstones and the basement (white dashed arrows in Fig. 15a). Brine circulation within deep fractured clastic rocks and/or the underlying fractured basement are well known for instance in the Upper Rhine Graben (Guillou-Frottier et al., 2013) and in the Limagne Basin (Calcagno et al., 2014). However, these contributions at Luhoi must be low, otherwise the geothermometer estimations should indicate higher temperatures.

6. Conclusions

In Fig. 15a we have qualitatively derived the permeability

distribution at Luhoi from the formations' porosity, assuming proportionality between them. In this hypothesis, the Luhoi geothermal field can be modelled as a three layers structure (Fig. 15a) made by a highly permeable medium (light grey) sandwiched between an overlying low-permeability clay cap and underlying low-permeability formations (dark grey). The higher permeability layer is made by the Kipatimu sandstones that hosts waters flowing in the regional hydrological circuit with temperature enhanced by the expected slightly anomalous regional gradient of the order of 41 °C/km (Fig. 15b, light grey line). At the top, the sandstone permeable layer is sealed regionally by the low-permeability claystone layer or, at Luhoi, by the shallow clay-rich sandstones imaged by the clay cation exchange capacity (CEC) distribution derived from the 3D magnetotelluric resistivity model. The regional gradient is likely altered by convective phenomena (Fig. 15b, blue line RT) and by the thermal conductivity variations of the stratigraphic column. The continuous clay cap layer has a higher temperature gradient consistent with conduction. Convection likely affects the permeable sandstone layer giving a reduced vertical gradient similarly to the temperature-depth graphs at the nearby wells (Fig. 2); similar small-scale convection superimposed on large-scale regional lateral flow of pore fluid has been described for instance in the Salton Sea geothermal field, which is also hosted in clastic sedimentary rocks, although temperatures are much higher (Younker et al., 1981). At the base of the sandstones layer (at a depth of ca. 2 km in the region outside Luhoi) the expected temperature reaches 100 °C, i.e. our estimated maximum reservoir temperature from water geothermometers. At Luhoi, the local horst structure imaged by the gravimetric 3D model pushes up the permeable sandstone layer of about 1 km and makes it to intersect the topographical surface. This causes a local up-doming of the regional isotherms and strongly increases the local geothermal gradient (Fig. 15b, red line LT). Up-doming of isotherms is also likely favored by convection related to the enhanced permeability due to fracturing along the normal faults. As result, the reservoir depth at Luhoi is of the order of 500 m with a very high expected local geothermal gradient. Manifestations occur along the NW edge of the asymmetric horst, where i) a larger number of NE trending faults enhances the secondary permeability, ii) WNW trending faults intersect the NE trending faults likely increasing porosity and iii)

the claystone layer is thinner.

The Luhoi geothermal play is therefore reminiscent of an extensional type play in a tectonically active intra-continental rift (Moeck, 2014), similarly to the Alalobeda geothermal system (Stimac et al., 2014; Rizzello et al., 2016; Pasqua et al., 2016) in the Tendaho Graben (northern Ethiopia) or the Mbaka system (Rizzello et al., 2018) in Southwest Tanzania. While most of the other studied geothermal systems along the East African Rift System (EARS) are of volcanic or plutonic type (e.g. Teklemariam Zemedkun, 2018), Luhoi is an example of probably the most diffuse geothermal resource type in the EARS, i.e. low to intermediate temperature, low enthalpy systems at shallow depth largely available for direct use applications (e.g. Lund and Boyd, 2016) and/or electricity generation using a binary fluids cycle (e.g. Moya et al., 2018).

CRediT authorship contribution statement

Egidio Armadillo: Conceptualization, Methodology, Software, Formal analysis, Writing - review & editing. **Daniele Rizzello:** Conceptualization, Methodology, Data curation, Investigation, Writing - review & editing. **Claudio Pasqua:** Funding acquisition, Conceptualization, Project administration, Investigation. **Paolo Pisani:** Funding acquisition, Conceptualization, Supervision. **Alessandro Ghirotto:** Resources, Visualization, Investigation. **Kato Kabaka:** Funding acquisition, Project administration. **Taramaeli Mnjokava:** Project administration. **Jonas Mwano:** Investigation. **Makoye Didas:** Resources, Visualization, Investigation. **Lucas Tumbu:** Investigation.

Declaration of Competing Interest

The authors declare that they have no known competing financial interests or personal relationships that could have appeared to influence the work reported in this paper.

Acknowledgements

This work has been supported by the Icelandic International Development Agency (ICEIDA), the Nordic Development Fund (NDF) and the Tanzania Geothermal Development Company (TGDC) under the auspices of the African Rift Geothermal Development Facility (ARGeo) and UNEP. Luigi Marini leaded the new geochemical survey, performed the geochemical data processing and interpretations and kindly reviewed an early version of the manuscript. TGDC team conducted the geophysical survey in collaboration with ELC-Electroconsult, Tellus and DISTAV. Gylfi Páll Hersir reviewed geophysical data acquisition, processing and modelling. Two anonymous reviewers improved the original manuscript. ASTER GDEM is a product of NASA and METI. SRTM data are USGS Products distributed by the Land Processes Distributed Active Archive Center (LP DAAC), located at USGS/EROS, Sioux Falls, SD (<http://lpdaac.usgs.gov>).

References

- Amante, C., Eakins, B.W., 2009.ETOPO1 1 arc-minute global relief model: procedures, data sources and analysis. NOAA Technical Memorandum NESDIS NGDC-24.
- National Geophysical Data Center, Marine Geology and Geophysics Division, Boulder, Colorado Available online at: <https://www.ngdc.noaa.gov/mgg/global/relief/ETOPO1/docs/ETOPO1.pdf>.
- Armadillo, E., Rizzello, D., Stimac, J., Zemedkun, M., Kebede, S., Mengiste, A., 2016. The ARGeo geophysical model of the Tendaho geothermal field, Ethiopia. In: Proceedings of the European Geothermal Congress. European Geothermal Congress 2016. Strasbourg, 19-23 September 2016. ISBN: 978-2-9601946-0-9.
- Arnason, K., Eysteinsson, H., Hersir, G.P., 2010. Joint 1D inversion of TEM and MT data and 3D inversion of MT data in the Hengill area, SW Iceland. Geothermics 39, 13–34. <https://doi.org/10.1016/j.geothermics.2010.01.002>.
- Battistelli, A., Amdeberhan, Y., Calore, C., Ferragina, C., Abatnesh, W., 2002. Reservoir engineering assessment of Dubti geothermal field, Northern Tendaho Rift, Ethiopia. Geothermics 31 (3), 381–406. [https://doi.org/10.1016/S0375-6505\(01\)00039-6](https://doi.org/10.1016/S0375-6505(01)00039-6).
- Blakely, R.J., 1995. Potential Theory in Gravity and Magnetic Applications. Cambridge University Press, Cambridge (UK) ISBN 0-521-41508-X.
- Bonté, D., Guillou-Frottier, L., Garibaldi, C., Bourgine, B., Lopez, S., Bouchot, V., Lucaleau, F., 2010. Subsurface temperature maps in French sedimentary basins: new data compilation and interpolation. Bull. Soc. Géol. Fr. 181 (4), 377–390.
- Bonvalot, S., Balmino, G., Briais, A., Kuhn, M., Peyrefitte, A., Vales Biancale, R., Gabalda, G., Moreaux, G., Reinquin, F., Sarraihl, M., 2012. World Gravity Map, 1:50000000 Map. BGI-CGMW-CNRS-IRD, Paris.
- Bowles-Martinez, E., Schultz, A., 2020. Composition of magma and characteristics of the hydrothermal system of Newberry Volcano, Oregon, from magnetotellurics. Geochim. Geophys. Geosystems 21^{https://doi.org/10.1029/2019GC008831}. e2019GC008831.
- Brownfield, M.E., 2016. Assessment of undiscovered oil and gas resources of the Tanzania Coastal Province, East Africa. In: Brownfield, M.E. (Ed.), Compiler, Geologic Assessment of Undiscovered Hydrocarbon Resources of Sub-Saharan Africa: U.S. Geological Survey Digital Data Series 69–GG, Chap. 12, <https://doi.org/10.3133/ds69GG>. 12 p.
- Bujakowski, W., Barbacki, A., Czerwińska, B., Pajak, L., Pussak, M., Stefaniuk, M., Trześniowski, Z., 2010. Integrated seismic and magnetotelluric exploration of the Skieriewice, Poland, geothermal test site. Geothermics 39 (1), 78–93. <https://doi.org/10.1016/j.geothermics.2010.01.003>.
- Calcagno, P., Baujard, C., Guillou-Frottier, L., Dagallier, A., Genter, A., 2014. Estimation of the deep geothermal potential within the Tertiary Limagne basin (French Massif Central): an integrated 3D geological and thermal approach. Geothermics 51, 496–508. <https://doi.org/10.1016/j.geothermics.2014.02.002>.
- Caldwell, T.G., Bibby, H.M., Caldwell, C., 2004. The magnetotelluric phase tensor. Geophys. J. Int. 158, 457–469.
- Chang, P.Y., Lo, W., Song, S.R., Ho, K.R., Wu, C.S., Chen, C.S., Lai, Y.C., Chen, H.F., Lu, H.Y., 2014. Evaluating the Chingshui geothermal reservoir in northeast Taiwan with integrated geophysical visualization model. Geothermics 50, 91–100. <https://doi.org/10.1016/j.geothermics.2013.09.014>.
- Clark, I.D., Fritz, P., 1997. Environmental Isotopes in Hydrogeology. CRC press 342 pp.
- Cumming, W., 2009. Geothermal resource conceptual models using surface exploration data. In: Proceedings of the Thirty-Fourth Workshop on Geothermal Reservoir Engineering. Stanford University, Stanford, California, February 9–11, 2009.
- Cumming, W., Mackie, R., 2010. Resistivity imaging of geothermal resources using 1D, 2D and 3D inversion and TDEM static shift correction illustrated by Glass Mountain Case History. In: Proceedings of the World Geothermal Congress. Bali, Indonesia, April 2010, 25–29.
- Daly, R.A., Manger, G.E., Clark, S.P., 1966. Density of rocks. In: Clark, S.P. (Ed.), Handbook of Physical Constants. GSA Memoirs. Geological Society of America, pp. 97.
- Didana, Y.L., Thiel, S., Heinsohn, G., 2015. Three dimensional conductivity model of the Tendaho High Enthalpy Geothermal Field, NE Ethiopia. J. Volcanol. Geotherm. Res. 290, 53–62. <https://doi.org/10.1016/j.jvolgeores.2014.11.013>.
- Egbert, G.D., Kelbert, A., 2012. Computational recipes for electromagnetic inverse problems. Geophys. J. Int. 189 (1), 251–267.
- Faulds, J.E., Bouchot, V., Moeck, I., Oguz, K., 2009. Structural controls of geothermal systems in western Turkey: a preliminary report. Geotherm. Resour. Coun. Trans. 33, 375–383.
- Faulds, J.E., Coolbaugh, M., Bouchot, V., Moeck, I., Oguz, K., 2010. Characterizing structural controls of geothermal reservoirs in the Basin and range, USA, and western Turkey: developing successful exploration strategies in extended terranes. In: Proceedings of the WGC. Bali, Indonesia, 2010. pp. 25–30 1163.
- Flóvenz, Ó.G., Spangenberg, E., Kulenkampff, J., Árnason, K., Karlssdóttir, R., Huenges, E., 2005. The role of electrical interface conduction in geothermal exploration. In: Proceedings of the World Geothermal Congress. Antalya, Turkey, 24–29 April 2005.
- Freymark, J., Sippel, J., Scheck-Wenderoth, M., Bär, K., Stiller, M., Fritsche, J.G., Kracht, M., 2017. The deep thermal field of the Upper Rhine Graben. Tectonophysics 694, 114–129. <https://doi.org/10.1016/j.tecto.2016.11.013>.
- Gamble, T.D., Gouba, W.M., Clarke, J., 1979. Magnetotellurics with a remote magnetic reference. Geophysics 44, 53–68.
- Grim, R.E., 1953. Clay Mineralogy. McGraw Hill, New York 384 pp.
- Guillou-Frottier, L., Carré, C., Bourgine, B., Bouchot, V., Genter, A., 2013. Structure of hydrothermal convection in the Upper Rhine Graben as inferred from corrected temperature data and basin-scale numerical models. J. Volcanol. Geotherm. Res. 256, 29–49. <https://doi.org/10.1016/j.jvolgeores.2013.02.008>.
- Hanson, R.E., 2003. Proterozoic geochronology and tectonic evolution of southern Africa. Geol. Soc. Lond. Spec. Publ. 206, 427–463.
- Hersir, G.P., Kristinsson, S.G., Mnjokava, T., 2015. Tanzania Visit in January 2015. Assessment of Areas for Surface Exploration Studies and Training Needs. Prepared for TGDC with Funding From ICEIDA. Iceland GeoSurvey, Report, ISOR-2015/025. 48 pp..
- Hochstein, M.P., Temu, E.B., Moshy, C.M.A., 2000. Geothermal resources of Tanzania. In: Proceedings of the World Geothermal Congress 2000. Kyushu-Tohoku, Japan.
- Horváth, F., Musitz, B., Balázs, A., Végh, A., Uhrin, A., Nádor, A., Koroknai, B., Pap, N., Tóth, T., Wórum, G., 2015. Evolution of the Pannonian basin and its geothermal resources. Geothermics 53, 328–352. <https://doi.org/10.1016/j.geothermics.2014.07.009>. ISSN 0375-6505.
- JICA, 2014. Data Collection Survey on Geothermal Energy Development in East Africa. Final Report (Tanzania). Available online at: Japan International Cooperation Agency Publications. <http://open.jicareport.jica.go.jp/pdf/12147823.pdf>.
- Jiracek, G.R., 1990. Near-surface and topographic distortions in electromagnetic induction. Surv. Geophys. 11 (2–3), 163–203. <https://doi.org/10.1007/BF01901659>.
- Jones, A.G., Jodicke, H., 1984. Magnetotelluric transfer function estimation improvement by a coherence-based rejection technique. In: Paper Presented at 54th Annual International Meeting, Soc. of Expl. Geophys. Atlanta, Ga., Dec. 2–6, 1984.

- Kabaka, K.T., Mnjokava, T.T., Kajugus, S.I., 2016. Geothermal development in Tanzania, a country update. In: Proceedings of the 6th African Rift Geothermal Conference. Addis Ababa, Ethiopia.
- Kajato, H., 1982. Gas strike spurs search for oil in Tanzania. *Oil Gas J.* 123, 123–131.
- Kapilima, S., 2002. Tectonic and sedimentary evolution of the coastal basin of Tanzania during the mesozoic times. *Tanz. J. Sci.* 29 (1), 1–16. <https://doi.org/10.4314/tjs.v29i1.18362>.
- Kelbert, A., Meqbel, N., Egbert, G.D., Tandon, K., 2014. ModEM: a modular system for inversion of electromagnetic geophysical data. *Comput. Geosci.* 66, 40–53.
- Keller, G.V., 1989. Electrical properties. In: Carmichael, R.S. (Ed.), *Practical Handbook of Physical Properties of Rocks and Minerals*. CRC Press, Boca Raton, Florida, pp. 359–427.
- Kent, P.E., Hunt, J.A., Johnstone, D.W., 1971. The Geology and Geophysics of Coastal Tanzania. Geophysical Paper N. 6. Her Majesty's Stationery Office (HMSO), London.
- Kraml, M., Kaudse, T., Mujumba, J., Leible, D., Aeschbach-Hertig, W., Kreuter, H., GPT Exploration Team, 2014. Geochemical and isotopic results of recent surface exploration in Rufiji area, Tanzania. In: Proceedings of the 5th African Rift Geothermal Conference. Arusha, Tanzania.
- Lanson, B., Beaufort, D., Berger, G., Bauer, A., Cassagnabere, A., Meunier, A., 2002. Authigenic kaolin and illitic minerals during burial diagenesis of sandstones: a review. *Clay Miner.* 37 (1), 1–22.
- Le Gall, B., Gernigon, L., Rolet, J., Ebinger, C., Gloaguen, R., Nilsen, O., Dypvik, H., Deffontaines, B., Mruma, A., 2004. Neogene-Holocene rift propagation in central Tanzania: Morphostructural and aeromagnetic evidence from the Kilombero area. *GSA Bulletin* 116 (3/4), 490–510. <https://doi.org/10.1130/B25202.1>.
- Lévy, L., Gibert, B., Sigmundsson, F., Flóvenz, Ó.G., Hersir, G.P., Briole, P., Pezard, P.A., 2018. The role of smectites in the electrical conductivity of active hydrothermal systems: electrical properties of core samples from Krafla volcano. Iceland. *Geophys. J. Int.* 215, 1558–1582. <https://doi.org/10.1093/gji/ggy342>.
- Li, C.F., Lu, Y., Wang, J., 2017. A global reference model of Curie point depths based on EMAG2. *Sci. Rep.* 7, 45129. <https://doi.org/10.1038/srep45129>.
- Lichoro, C.M., Árnason, K., Cumming, W., 2017. Resistivity imaging of geothermal resources in northern Kenya rift by joint 1D inversion of MT and TEM data. *Geothermics* 68, 20–32. <https://doi.org/10.1016/j.geothermics.2017.02.006>.
- Lichoro, C.M., Árnason, K., Cumming, W., 2019. Joint interpretation of gravity and resistivity data from the Northern Kenyavolcanic rift zone: structural and geothermal significance. *Geothermics* 77, 139–150. <https://doi.org/10.1016/j.geothermics.2018.09.006>.
- Lund, J.W., Boyd, T.L., 2016. Direct utilization of geothermal energy 2015 worldwide review. *Geothermics* 60, 66–93. <https://doi.org/10.1016/j.geothermics.2015.11.004>.
- Mbede, E.I., Dualah, A., 1997. The coastal basins of Somalia, Kenya, and Tanzania. In: In: Selley, R.C. (Ed.), *African Basins-Sedimentary Basins of the World Vol. 3*. Elsevier Science B. V., Amsterdam, pp. 211–233.
- McKenna, J.R., Blackwell, D.D., 2004. Numerical modeling of transient Basin and Range extensional geothermal systems. *Geothermics* 33, 457–476. <https://doi.org/10.1016/j.geothermics.2003.10.001>.
- Meju, M., 1996. Joint inversion of TEM and distorted MT soundings: some effective practical considerations. *Geophysics* 61, 56–65.
- Meqbel, N., 2009. The Electrical Conductivity Structure of the Dead Sea Basin Derived from 2D and 3D Inversion of Magnetotelluric Data. PhD Thesis. Free University of Berlin, Berlin, Germany.
- Meyer, B., Saltus, R., Chulliat, A., 2017. EMAG2: Earth Magnetic Anomaly Grid (2-arc-minute resolution) Version 3. National Centers for Environmental Information, NOAA. <https://doi.org/10.7289/V5H70CVX>.
- Mnjokava, T., Kabaka, K., Mayalla, J., 2015. Geothermal development in Tanzania – a Country update. In: Proceedings of the World Geothermal Congress 2015. Melbourne, Australia.
- Moeck, I.S., 2014. Catalog of geothermal play types based on geologic controls. *Renew. Sustain. Energy Rev.* 37, 867–882. <https://doi.org/10.1016/j.rser.2014.05.032>.
- Moya, D., Aldásd, C., Kaparajué, P., 2018. Geothermal energy: power plant technology and direct heat applications. *Renew. Sustain. Energy Rev.* 94, 889–901. <https://doi.org/10.1016/j.rser.2018.06.047>.
- Mpanda, S., 1997. Geological Development of the East African Coastal Basin of Tanzania (dissertation). Stockholm University, Dept. of Geology and Geochemistry, Stockholm, Sweden.
- Muffler, L.J.P., White, D.E., 1969. Active metamorphism of Upper Cenozoic sediments in the salton Sea geothermal field and the Salton Trough, Southeastern California. *Geol. Soc. Am. Bull.* 94, 161–180.
- Mulibio, G.D., Nyblade, A.A., 2016. The seismotectonics of Southeastern Tanzania: Implications for the propagation of the eastern branch of the East African Rift. *Tectonophysics* 674, 20–30. <https://doi.org/10.1016/j.tecto.2016.02.009>.
- Múnoz, G., 2014. Exploring for geothermal resources with electromagnetic methods. *Surv. Geophys.* 35, 101–122. <https://doi.org/10.1007/s10712-013-9236-0>.
- Múnoz, G., Ritter, O., Moeck, I., 2010a. A target-oriented magnetotelluric inversion approach for characterizing the low enthalpy Groß Schönebeck geothermal reservoir. *Geophys. J. Int.* 183, 1199–1215. <https://doi.org/10.1111/j.1365-246X.2010.04795.x>.
- Múnoz, G., Bauer, K., Moeck, I., Schulze, A., Ritter, O., 2010b. Exploring the Groß Schönebeck (Germany) geothermal site using a statistical joint interpretation of magnetotelluric and seismic tomography models. *Geothermics* 39 (1), 35–45. <https://doi.org/10.1016/j.geothermics.2009.12.004>.
- NASA/METI/AIST/Japan Spacesystems, and U.S./Japan ASTER Science Team, 2009. ASTER Global Digital Elevation Model. NASA EOSDIS Land Processes DAAC. <https://doi.org/10.5067/ASTER/ASTGTM.002>.
- Nzaro, M.A., 1970. Geothermal resources of Tanzania. *Geothermics* 2, 1039–1043. [https://doi.org/10.1016/0375-6505\(70\)90412-8](https://doi.org/10.1016/0375-6505(70)90412-8).
- O'Donnell, J.P., Adams, A., Nyblade, A.A., Mulibio, G.D., Tugume, F., 2013. The uppermost mantle shear wave velocity structure of eastern Africa from Rayleigh wave tomography: constraints on rift evolution. *Geophys. J. Int.* 194 (2), 961–978. <https://doi.org/10.1093/gji/ggt135>.
- Ogawa, Y., 2002. On two-dimensional modeling of magnetotelluric field data. *Surv. Geophys.* 23 (2-3), 251–273.
- Parker, R.L., 1972. The rapid calculations of potential anomalies. *Geophys. J. R. Astr. Soc.* 31, 447–455.
- Parkinson, W.D., 1959. Direction of rapid geomagnetic fluctuations. *Geophys. J. 2*, 1–14.
- Pasqua, C., Armadillo, E., Rizzello, D., Verdoya, M., Chiozzi, P., Kebede, S., 2016. Integrated analysis of geochemical and geophysical data from Alalobeda geothermal field, Northern Afar Region. In: Proceedings of the 6th African Rift Geothermal Conference. Addis Ababa.
- Reid, A.B., Allsop, J.M., Granser, H., Millet, A.J., Somerton, I.W., 1990. Magnetic interpretation in three dimensions using Euler deconvolution. *Geophysics* 55 (1), 80–91.
- Rizzello, D., Armadillo, E., Verdoya, M., Pasqua, C., Kebede, S., Mengiste, A., Abera, N., 2016. Integrated geophysical imaging of the Alalobeda geothermal field (Ethiopia). In: Proceedings of the European Geothermal Congress. Strasbourg. ISBN: 978-2-9601946-0-9.
- Rizzello, D., Armadillo, E., Pasqua, C., Pisani, P., Mnjokava, T., Mwano, J., Didas, M., Tumbu, L., 2018. Three-dimensional geophysical modelling of Kiejo-Mbaka geothermal field, Tanzania. Proceedings of the 7th African Rift Geothermal Conference.
- Said, A., Moder, C., Clark, S., Abdelmalak, M.M., 2015. Sedimentary budgets of the Tanzania coastal basin and implications for uplift history of the East African rift system. *J. Afr. Earth Sci.* 111, 288–295.
- Scheck-Wenderoth, M., Maystrenko, Y.P., 2013. Deep control on shallow heat in sedimentary basins. *Energy Procedia* 40, 266–275.
- Schön, J.H., 1996. Physical properties of rocks – fundamentals and principles of petrophysics. *Handbook of Geophysical Exploration: Seismic Exploration*, 18. Pergamon Press.
- Spector, A., Grant, F.S., 1970. Statistical models for interpreting aeromagnetic data. *Geophysics* 35 (2), 293–302.
- Stamps, D.S., Saria, E., Kreemer, C., 2018. A geodetic strain rate model for the east african rift system. *Sci. Rep.* 8, 732. <https://doi.org/10.1038/s41598-017-19097-w>.
- Sternberg, B.K., Washburne, J.C., Pellerin, L., 1988. Correction for the static shift in magnetotellurics using transient electromagnetic soundings. *Geophysics* 53, 1459–1468.
- Stimac, J., Armadillo, E., Kebede, S., Zemedkun, M., Kebede, Y., Teclu, A., Rizzello, D., Mandeno, P.E., 2014. Integration and modeling of geoscience data from the Tendaho Geothermal Area, Afar Rift, Ethiopia. In: Proceeding of the Fifth African Rift Geothermal Conference. Arusha, Tanzania.
- Sutarno, D., 2008. Constrained robust estimation of magnetotelluric impedance functions based on a bounded-influence regression M-estimator and the Hilbert transform. *Nonlin. Processes Geophys.* 15, 287–293.
- SWECO, 1978. Reconnaissance of Geothermal Resources. Report for the Ministry of Water, Energy and Minerals of Tanzania. SWECO, Stockholm.
- Szanyi, J., Kovács, B., 2010. Utilization of geothermal systems in South-East Hungary. *Geothermics* 39 (4), 357–364. <https://doi.org/10.1016/j.geothermics.2010.09.004>.
- Teklemariam Zemedkun, M., 2018. Geothermal outlook in East Africa and contribution of UNU-GTP in capacity building. In: United Nations University Geothermal Training Programme 40th Anniversary Workshop. Reykjavik, Iceland, April 26, 2018. available online at: <https://orkustofnun.is/gogn/unu-gtp-40-ann/UNU-GTP-40-A-1-Meseret-Teklemariam.pdf>.
- Ussher, G., Harvey, C., Johnstone, R., Anderson, E., 2000. Understanding the resistivities observed in geothermal systems. In: Proceedings of the World Geothermal Congress 2000. Kyushu - Tohoku, Japan, May 28 - June 10, 2000.
- Waxman, M.H., Smits, L.J.M., 1968. Electrical Conductivities in Oil-Bearing Shaly Sands. *Soc. Pet. Eng. J.* 107–122, 243 Trans. AIME.
- Worden, R.H., Morad, S., 2003. Clay minerals in sandstones: controls on formation, distribution and evolution. *Int. Assoc. Sedimentol.* 34, 3–41. <https://doi.org/10.1002/9781444304336.ch1>. Special Publication.
- Younker, L.W., Kasameyer, P.W., Tewhey, J.D., 1981. Geological, geophysical, and thermal characteristics of the Salton Sea Geothermal Field, California. *J. Volcanol. Geotherm. Res.* 12 (3–4), 221–258. [https://doi.org/10.1016/0377-0273\(82\)90028-2](https://doi.org/10.1016/0377-0273(82)90028-2).
- Zhou, Z., Tao, Y., Li, S., Ding, W., 2013. Hydrocarbon potential in the key basins in the East Coast of Africa. *Petrol. Explor. Develop.* 40 (5), 582–591.